The Sub-mm Emission of a Major Galaxy Merger

Christina Knudsen

Thesis submitted for the degree of
Master of Science in Astronomy

Institute of Theoretical Astrophysics
University of Oslo

1st June 2021

Abstract

Galaxy mergers play a fundamental role in the hierarchical model of galaxy evolution. They are also thought to be an important process in fueling the growth of supermassive black holes (SMBH) and thus powering active galactic nuclei (AGN) activity. NGC6240 is a local merger and luminous infrared galaxy (LIRG). It has two AGNs in its center, and it shows massive molecular outflows extending by > 10 kpc. The aim of this work is to study the cold dust emission in NGC6240 both in the nuclear region (affected by vigorous starburst and AGN activity) and in an extended region (affected by outflows and tidal tails). This is done by exploiting high sensitivity archival ALMA datasets at observed frequencies ranging from 84 GHz ($\lambda \sim 3$ mm) to 680 GHz ($\lambda \sim 0.4$ mm).

The first result of my work is the detection of a significant amount of emission beyond the central 1.5 kpc region, which was the portion of the galaxy on which most previous interferometric studies have focused. This extended component represents 32% of the total emission measured within the frequency range 336.6-352.2 GHz. Since these single-pointing interferometric observations have a limited field of view (FoV 63" in band 3, but only 22" in band 9) and therefore are not sensitive to larger scales, the extended emission contribution could be considered a lower limit. The shape of the extended emission I detect is spatially correlated with the blueshifted and redshifted components of the molecular outflow studied in [CI] and CO by previous works.

I have also identified three new point sources. Two of them are found in between the two AGNs which i have labelled C-4 and C-3. C-4 is at the midpoint between the two AGNs, while C-3 is closer to the southern nucleus. The position of C-4 coincides with the peak of the redshifted [CI] outflow, and the position of C-3 is close to the peak of the blueshifted [CI] outflow. This suggests that the outflow is closely related to the source that heats the dust in this region. The third source, labelled C-11, is found in the north-east ~ 4.3 kpc from the northern AGN at Ra = 16:52:59.256 and Dec = 02.24.11.458.

I have compared my (sub)mm continuum flux measurements from the nuclear and extended region and from the five point sources (the two AGNs and three new sources detected in this work) with a model for the spectral energy distribution (SED) and previous observations of this galaxy. Unfortunately, the new data are insifficient to perform a detailed SED fitting, but I have robustly detected some differences in the low-frequency part of the SED (at 1-3 mm). In particular, for the box probing the extended continuum emission I find a flux increase from the datapoints at 130 GHz to 97 GHz. This long wavelength part of the SED is often associated with AGN activity,

but it has been suggested that this emission may also be attributed to synchrotron emission from outflows. The rising trend and the cospatiality between the molecular outflow and these extended continuum features support this hypothesis. From the SED of C-3 and C-4, I find that both point sources have a SED that resembles that of the two known AGNs. C-3 also has a counterpart in the radio (VLBI observations at 5 GHz), which suggests that this might be an additional obscured AGN. However, with the current data, I cannot rule out that C-3 and C-4 are starburst regions. The source C-11 does not follow the same rising slope at low frequencies in its SED, and does not have a counterpart in the X-ray, which suggests that it is unlikely an AGN. It may rather be a supernova or another nucleus. Since tidal dwarf galaxies (TDGs) have previously been observed in the tidal tails of gas rich mergers, and this work suggests that there are additional continuum sources outside the nuclear region, it is also possible that this source is a TDG.

The detection of extended emission spatially correlated with outflows in addition to three new point sources in NGC6240 gives greater insight into the origin of the (sub)-mm continuum emission, and may explain the extreme ISM of this galaxy. The possible detection of multiple nuclei in a local merger is of great importance both observationally, as the potential for observing obscured AGNs with (sub)-mm continuum emission is very promising, and also from a cosmological point of view, as this helps understanding the hierarchical model of galaxy evolution.

Future studies targeting line-free frequency ranges and with a higher sensitivity to larger scales will help us understand the origin of the sub-mm continuum emission in NGC6240. As there are few observations contributing to the long wavelength part of the SED of NGC6240, studies in the far-IR to radio would also contribute to constraining the SED further and give insight into the components that dominate at these wavelengths.

Acknowledgments

I want to thank my supervisor Claudia Cicone for giving me the opportunity to work on such an interesting project. I also want to thank Claudia for her insightful inputs and all the help, patience and support this year.

I also want to thank my family for the wholehearted support throughout my studies.

Contents

Chapter 1

Introduction

Galaxy mergers play an important role in the hierarchical model of galaxy evolution. The largest galaxies in the Universe have likely experienced several merging processes during their lifetime, and there are strong indications that elliptical galaxies are the end products of major mergers. During a merging process, redistribution of baryonic matter in the interstellar medium (ISM) is possible, and gravitational torques funnel gas towards the central region, triggering active galactic nuclei (AGNs) and starbursts. Many local (ultra) luminous infrared galaxies (ULIRGs) are interacting galaxies, and I will in this work study the local LIRG NGC6240. I will do this by analyzing the (sub)mm continuum emission using data from the Atacama Large Millimeter/submillimeter Array (ALMA). Previous interferometric studies have focused on the nuclear region of this merger, which hosts two AGNs, and so they might have missed important information from the extra-nuclear regions, where a prominent molecular outflow has been detected and other processes such as tidal tails or offset star formation activity can be at work. The aim of this work is to investigate these properties by studying both the nuclear and an extended region of this galaxy. In this chapter I will present the theoretical background for this work.

1.1 Galaxy Formation and Evolution

Cosmology defines the space-time frame and sets the initial conditions for galaxy formation and evolution. The modern cosmological paradigm is based on Einstein's theory of General Relativity (GR) and the cosmological principle (Mo et al. (2010)). GR describes the geometry of space-time in the presence of matter and energy, and the cosmological principle states that the Universe is homogeneous and isotropic on large enough scales, supported by observational evidence, such as the large scale distribution of galaxies (Colless et al. (2001)) and the cosmic microwave background (CMB) radiation (de Bernardis et al. (2000)). In addition, the cosmic expansion is a fundamental ingredient to cosmological models. It was first observed by Hubble (Hubble (1929)). He found that the redshift (the shift of light to longer wavelengths) of galaxies was directly proportional with the distance from us. The Hubble law can be written as

$$v = H_0 D = cz, \tag{1.1}$$

where H_0 is the Hubble constant, D is the distance from us, and the redshift z is defined as

$$z \equiv \frac{\lambda_{obs}}{\lambda_{em}} - 1 = \frac{v}{c}. \tag{1.2}$$

The evolution of the Universe is fully determined by its geometrical curvature and its mass and energy content (Mo et al. (2010)). The mass-energy density has three components: the non-relativistic matter energy density (mainly cold dark matter (CDM)), the radiation energy density, and the dark energy (an energy connected to the cosmological constant Λ). Each of these corresponds to a density parameter Ω_i which together with the Hubble constant make up the cosmological parameters in the first Friedman equation:

$$H(t)^2 = H_0(\frac{\Omega_{r,0}}{a^4} + \frac{\Omega_{m,0}}{a^3} + \Omega_{\Lambda,0} - \frac{\Omega_{tot} - 1}{a^2}), \tag{1.3}$$

which provides the Hubble parameter (the expansion rate of the Universe) as a function of the density parameters at the present time and the scaling factor $a(t) = \frac{1}{1+z(t)}$. These are all measurable parameters. The Planck satellite, launched in 2009, provided a detailed map of the CMB across the whole sky (apart from the region that is contaminated by our own Galactic plane), and allowed for a high precision measurement of the cosmological parameters (Ade et al. (2016)). These results revealed that the present Universe is dominated by Λ, constituting about 70% of the mass-energy, and that matter represents the remaining 30%, mainly in the form of CDM. This has motivated the reference to the commonly accepted cosmological model as the ΛCDM model.

1.1.1 Structure Formation

The Universe expands adiabatically,

$$TV^{\gamma-1} = constant, \tag{1.4}$$

where T is the temperature in a volume V and γ is the adiabatic index (Peacock (1999)). The cosmological volume expands under the effect of the scaling factor a as $V \propto a^3$ which gives $T \propto \frac{1}{a}$ for relativistic particles ($\gamma_{rel} = \frac{4}{3}$). This tells us that the Universe cools down during the expansion, and that the younger the Universe, the higher its temperature. In fact, this predicts an infinitely hot and dense Universe at $a(0) = 0$, known as the Big Bang singularity, occurring 13.7 Gyrs ago.

The first instants after Big Bang are known as the Planck era. No current theory is able to describe the Universe at this time, up to the Planck time $t_p \sim 5\text{x}10^{44}$ s. After this comes the Great Unification Theory epoch, where gravity separated from the unified force of the Standard Model (Witten (1981)). This epoch was succeeded by the Inflation (Guth (1981)). During the Inflation, the Universe experienced a sudden and instantaneous exponential expansion, where it increased its linear size by a factor of at

least 10^{26}. The time is now t $\sim 10^{-32}$. Nucleosynthesis, the formation of new atomic nuclei, started around 3 minutes after the Big Bang (Boesgaard and Steigman (1985)). Only the simplest reactions occurred, however, as the Universe cooled enough to halt the process after less than an hour. The Universe was left with about 75% hydrogen, 24% helium and some other elements such as lithium. For several hundred thousand years, the atoms were completely ionized due to the high temperature. At about 370 thousand years after the Big Bang, the temperature had decreased enough to bound electrons and protons, and photons decoupled from matter (Gott and Rees (1975)). This epoch is called the Recombination period and the photons from this time can be observed today as the CMB. The era after the Recombination is known as the Dark Ages (Barkana and Loeb (2001)), where there were no sources of light. During this time, small DM density perturbations started to grow. The era ended when baryons collapsed to form the first stars and galaxies. Then, at z $\sim$ 0.5 the dark energy dominated era began, which led to the accelerated expansion of the Universe we observe today (Perlmutter et al. (1999)).

Dark matter settles in gravitationally bound structures called DM halos. The standard theory of galaxy formation predicts that baryons are accreted into their potential wells (Barkana and Loeb (2001)). The infalling gas experiences a thermal shock during the accretion and is heated to the temperature in the DM halo. The baryon halo, embedded in the DM halo, is balanced against gravitational collapse by pressure support. Due to radiative processes, the gas halos cool, lose their pressure, and the gas falls towards the center of the halo, creating the galaxy disks (White and Rees (1978)). Then, gravitational instabilities of cold, dense gas clouds trigger collapse and eventually the formation of stars (Schmidt (1959)).

1.1.2 Star Formation Activity

The star formation history is one of the most fundamental observables in astronomy, and measurements of the star formation rate (SFR) can give insight to the evolution of baryonic structures in the Universe. Numerous studies of the star formation rate density (SFRD) have been conducted, and have established the SFRD evolution from z = 0 to the early Universe up to z $\sim$ 10 (Madau et al. (1996), Hopkins (2004), Steidel et al. (2004), Giavalisco et al. (2004), Hopkins et al. (2008), Bouwens et al. (2015), Drake et al. (2017)). From these observations we see that the SFR rises to a peak at z $\sim$ 2 and then rapidly drops by almost an order of magnitude until today (as shown in figure 1.1), showing that the Universe was a much more active place in the past. The SFR can be connected to other physical properties of galaxies, e.g. the stellar mass ($M_\star$), where a tight correlation between the SFR and $M_\star$ has been observed for star forming galaxies (Brinchmann et al. (2004), Peng et al. (2010)). The log($M_\star$) - log(SFR) plane exhibit a clear star forming sequence called the Main Sequence (MS), at which the majority of star forming galaxies lie (see figure 1.2).

Only a few percent of galaxies have a higher specific SFR (SSFR=SFR/$M_\star$) compared to the local main sequence and so lie above it in the SFR-$M_\star$ plane (Rodighiero et al. (2011)). These are called starburst galaxies. The evolution of the MS suggests that for the dominant population of star forming galaxies, the star formation histories

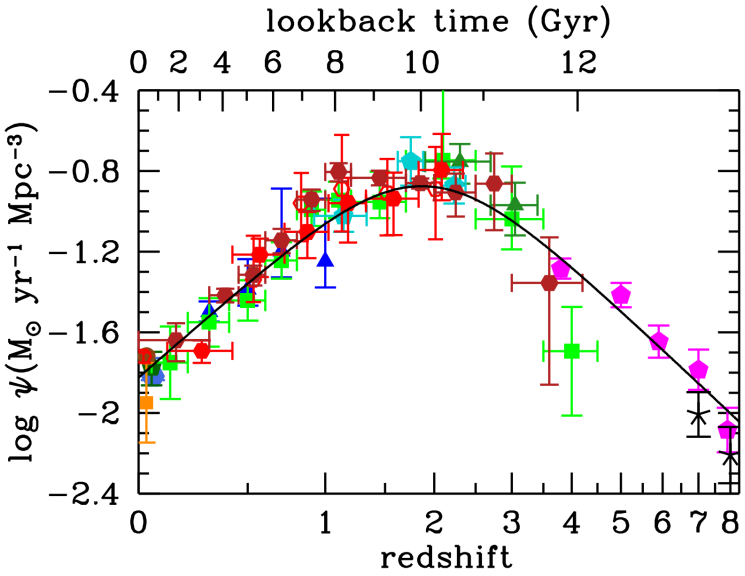

Figure 1.1: Cosmic star formation history from FUV and IR measurements. Figure from Whitaker et al. (2014).

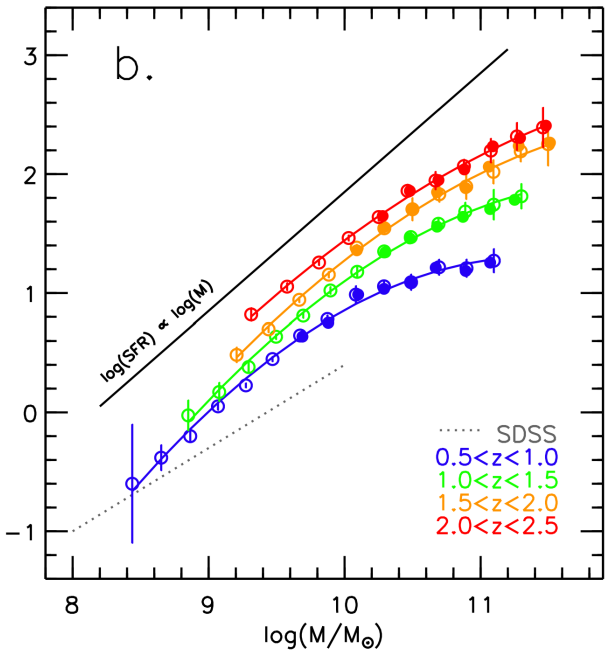

Figure 1.2: SFR as a function of stellar mass, with a redshift evolution. Figure from Whitaker et al. (2014).

are on average regular and continuous, and that the SFR increases by almost an order of magnitude at fixed $M_\star$ from $z \sim 0$ to $z \sim 2$.

To try to understand how galaxies grow with time, Schmidt (1959) looked at the relation between the SFR and the mass of the gas (M_{gas}) in the galaxy. This relation between the gas density (including both HI and H_2) and SFR is now called the Schmidt-Kennicutt law (Kennicutt (1998)). Later observations (Leroy et al. (2008), Bigiel et al. (2008)) demonstrated that the actual correlation is with only H_2. As stars form when gas cools and collapses, this relation indicates that what drives the MS evolution with redshift is the fuel available for SF, and that galaxies at high z were more gas rich than the local galaxies. However, without any external gas supply, the gas reservoir in normal galaxies would be consumed at a much shorter time scale than the age of the Universe (Daddi et al. (2010)), which has put forward the need for gas accretion by the intergalactic medium (IGM). Inflow from the IGM has therefore become a key ingredient of modern theoretical models of galaxy formation.

Starburst galaxies lie above the MS having a higher SFR per unit $M_\star$ (a higher SSFR), and are associated with different growth mechanisms than normal galaxies. While the SFR of MS galaxies is mainly driven by gas content which is in turn supplied by accretion from the IGM, starbursts are boosted by mergers of large galaxies, a theory supported by observations of local starburst galaxies (Sanders and Mirabel (1996)). Supporting this argument, the fraction of interacting galaxies has been found to increase systematically with distance from the MS (Hung et al. (2013)). Dynamical interactions can remove angular momentum and drive gas inflows towards the central region, and induce star formation. Galaxy mergers are also thought to play a fundamental role in fueling the growth of supermassive black holes (SMBH) and thus powering active galactic nuclei (AGN) activity.

1.1.3 Galaxy Merging

According to the ΛCDM model, DM halos form through mergers of smaller halos hierarchically, with the merger of the baryonic counterparts as a result (Somerville and Davé (2015)). It is suggested that merging is the dominant process in forming the most massive galaxies in the Universe, and Conselice (2007) estimated that massive galaxies likely have experienced 4-5 major mergers since $z \sim 3$. In the classical merger sequence, proposed by Sanders et al. (1988), quasars are the result of mergers of gas rich spirals. First, the merger leads to the formation of ultraluminous infrared galaxies (ULIRGs). The molecular gas flows into the nuclear region and provides fuel for the active galactic nuclei (AGN). The combined forces of supernova explosions and radiation pressure sweep the dust clear of the nuclear region, and the resulting object is an optical quasar. It has also been suggested that ULIRGs are the primary stage in the formation of elliptical galaxies (Hernquist (1992), Barnes (1988), Cattaneo (2001)).

As SMBHs are present in the center of most large galaxies (Ferrarese and Ford (2005)), and mergers are one of the main processes for driving the gas towards the nuclear region and thus triggering AGN activity, the formation of dual AGNs is expected in many of the merging or merged galaxies (Severgnini et al. (2021)). The dual AGN stage in a major merger is of great importance for galaxy evolution, as it is directly linked with rapid SMBH accretion and strong feedback effects (Veilleux et al. (2013)). The incidence of confirmed dual AGNs from observations is however very low compared with the merger rate (Springel et al. (2005), Capelo et al. (2017)). This may be due to observational biases such as wavelength coverage, incompleteness of the samples, and the resolution needed for the identification of pairs at small separations (Severgnini et al. (2021)). For example, a method for selecting dual AGN candidates is searching for double-peaked narrow optical emission line sources (McGurk et al. (2015)). This method does not however discern whether this emission comes from a double nucleus or kinematical effects occurring in a single AGN (Severgnini et al. (2021)). To further constrain this, searches for double peaks at different wavelengths and high resolution observations are needed.

Mergers shape the kinematic and physical properties of galaxies through gravitational torques and disruptions (Hopkins et al. (2008)). Tidal features that are generated in a merger strongly depend on both the mass ratio (minor or major merger) and gas fraction (gas rich or gas poor), in addition to internal structures and orbital parameters. They are therefore good tools to characterize a merger. Tidal *streams* are often detected in a minor merger where a satellite galaxy falls into a massive galaxy (Martínez-Delgado et al. (2010)), while tidal *tails* can be generated in major mergers between disks of equal size (Barnes and Hernquist (1992)).

Mergers between spheroidal galaxies, which are mostly gas poor and hot, are not accompanied by tidal features (or starbursts). Mergers between gas rich spiral galaxies, on the other hand, show features such as starbursts, AGN activity, and long tidal arms with stellar and gaseous material which can extend hundreds of kiloparsecs away from the parent galaxy. Tidal arms are formed during the encounter of the galaxies when strong tidal forces expel the material from their parent galaxies' disks. The resulting distribution of gas and stars in tidal tails can be very different, with some tails showing clear gaps - possibly a consequence of a local collapse or feedback (Hibbard and van Gorkom (1996)), and others showing an offset between the stellar and gaseous material (Hibbard and Yun (1999)). The amount of gas and stellar mass in tidal tails can be of several $10^9 M_\odot$. It was suggested early that new stellar systems could form in these tails (Zwicky (1956)), and such tidal dwarf galaxies (TDGs) have later been observed in several mergers (Ren et al. (2020)). Ren et al. (2020) estimated the production rate of these TDGs per major merger to be 0.36

In figure 1.4 I show snapshots from a simulation of the time evolution of a gas rich merger with SMBH by Di Matteo et al. (2005). Here we can see the characteristic tails at large distances. In this simulation, the gas eventually cools in the central region and reassembles in a disk component. See also figure 1.3 for a beautiful optical image of the local merger NGC6240, which is known for its butterfly shape and prominent tidal tails.

Figure 1.3: Hubble image of NGC6240. Field of view: $\sim$ 3 arcminutes. Credit: NASA, ESA, the Hubble Heritage (STScI/AURA)-ESA/Hubble Collaboration, and A. Evans (University of Virginia, Charlottesville/NRAO/Stony Brook University).

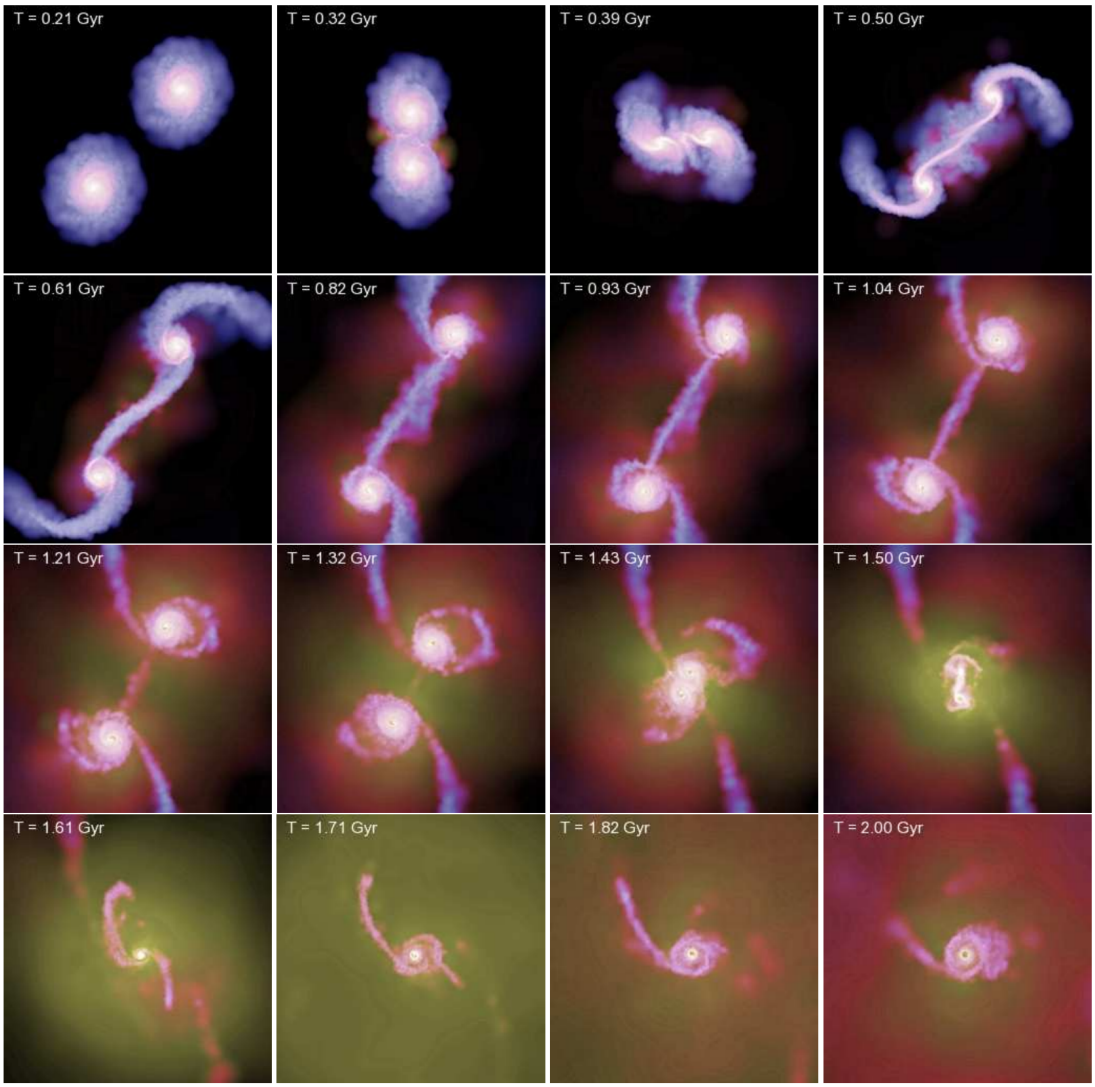

Figure 1.4: Snapshots of the time evolution of a simulated merger of two gas rich disk galaxies with SMGHs. A small disk component is reassembled in the remnant of this gas rich merger. Figure from Di Matteo et al. (2005).

1.1.4 AGN

Active galactic nuclei (AGN) are the most powerful, steady sourced objects in the Universe (Hickox and Alexander (2018)), with luminosities ranging from 10^6 - $10^{13} L_o$ (Fabian (1999)). AGNs are the observational signature of gas accretion onto supermassive black holes (SMBHs). This accretion produces an optically thick disk called the accretion disk. Due to the viscosity within the disk, it emits thermally at a wide range of temperatures. The emission is therefore spread across the electromagnetic spectrum, often peaking in the UV, but with significant luminosity in the infrared (IR) and X-ray bands. The disks are small and unresolved even for local AGNs.

For some AGNs, however, the emission from the accretion disk cannot be directly detected due to obscuration (Netzer (2015)). This occurs when gas or dust absorb or scatter the radiated emission. The source of obscuration is dominated by dust for the UV to IR wavelengths, and by gas for the X-ray wavelengths. The level of obscuration is also dependent on the wavelength, and regions with a high optical depth will absorb more emission.

According to the Unified Model of AGN (Urry and Padovani (1995)), see figure 1.5), the accretion disk is surrounded by an axisymmetric dusty and molecular structure, often called a dusty torus. The torus is optically thick and in some directions it completely obscures the central source. The peak of this component appears to be around $\lambda \sim 20 - 50 \mu$m with a steep fall off at longer wavelengths (Harrison (2014)).

Figure 1.6 shows a spectral energy distribution (SED) of an unobscured AGN. The observed power-law spectrum of high energy X-rays (cyan dotted line in figure 1.6) is thought to be due to an optically thin corona around the accretion disk (Harrison (2014)), where photons produced in the accretion disk experience Compton upscattering. This emission may also reflect off the torus or accretion disk to create a reflecting component in the X-ray (green line). In the soft X-ray region, the emission observed is higher than expected from accretion disk models, referred to as the soft excess component (magenta). An omnipresent component in the X-ray emission from AGNs is also a prominent Iron Kα emission line, peaking at 6.4 eV (Ricci et al. (2014)).

The luminosities at radio frequencies differ by several orders of magnitude from radio-loud to radio-quiet AGNs (Harrison (2014), Kellermann et al. (2004)). The radio emission in the radio-loud sources originates from oppositely directed, relativistic jets (Ghisellini (2013)), with the direction likely traced by the axis of a spinning black hole. Associated with the jets are radio lobes. These are very large structures (observations of the galaxy Centaurus A revealed lobes extending ~ 600 kpc (Stawarz et al. (2013))) that produce synchrotron radiation, created by particles at relativistic speeds that spiral in a magnetic field. In radio-quiet sources, the origin of the radio radiation is less certain, but likely related to compact radio jets, supernovae and a corona (Harrison (2014), Smith et al. (1998), Laor and Behar (2008)).

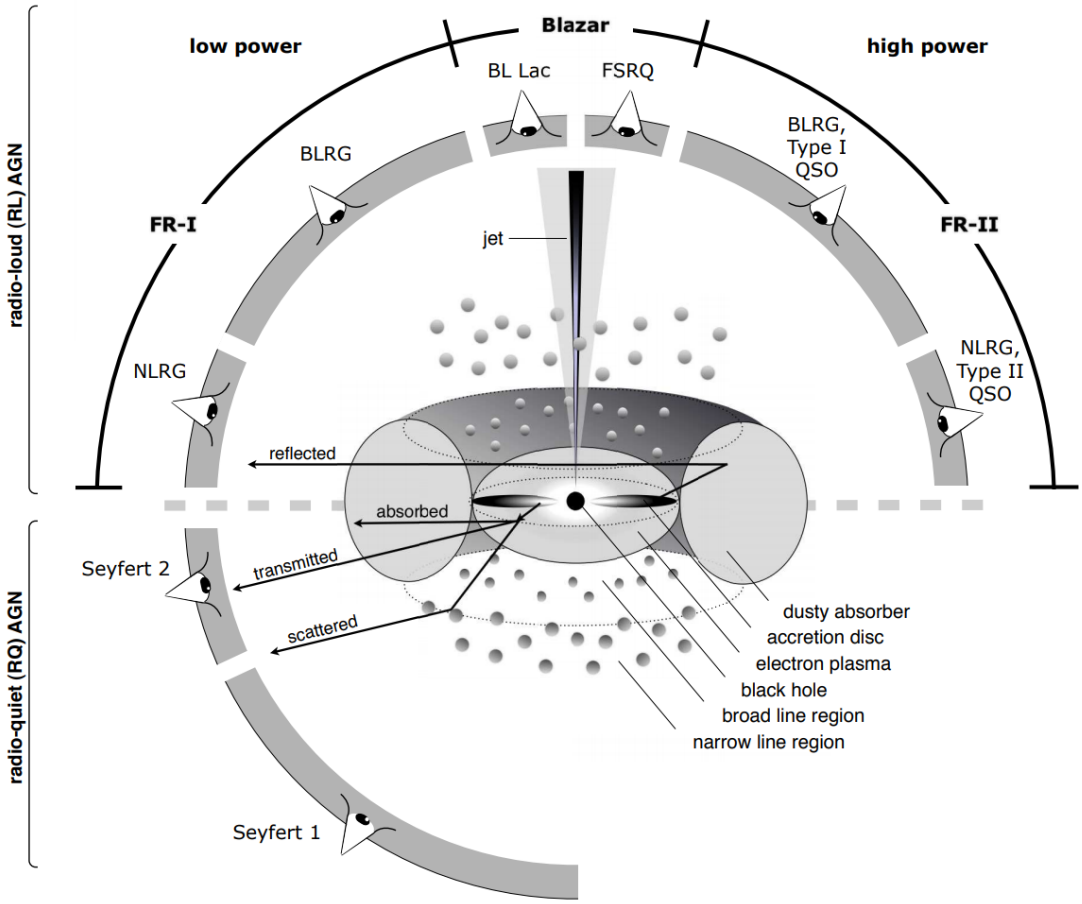

Figure 1.5: Schematic representation of the unified AGN model. Figure from Beckmann and Shrader (2013).

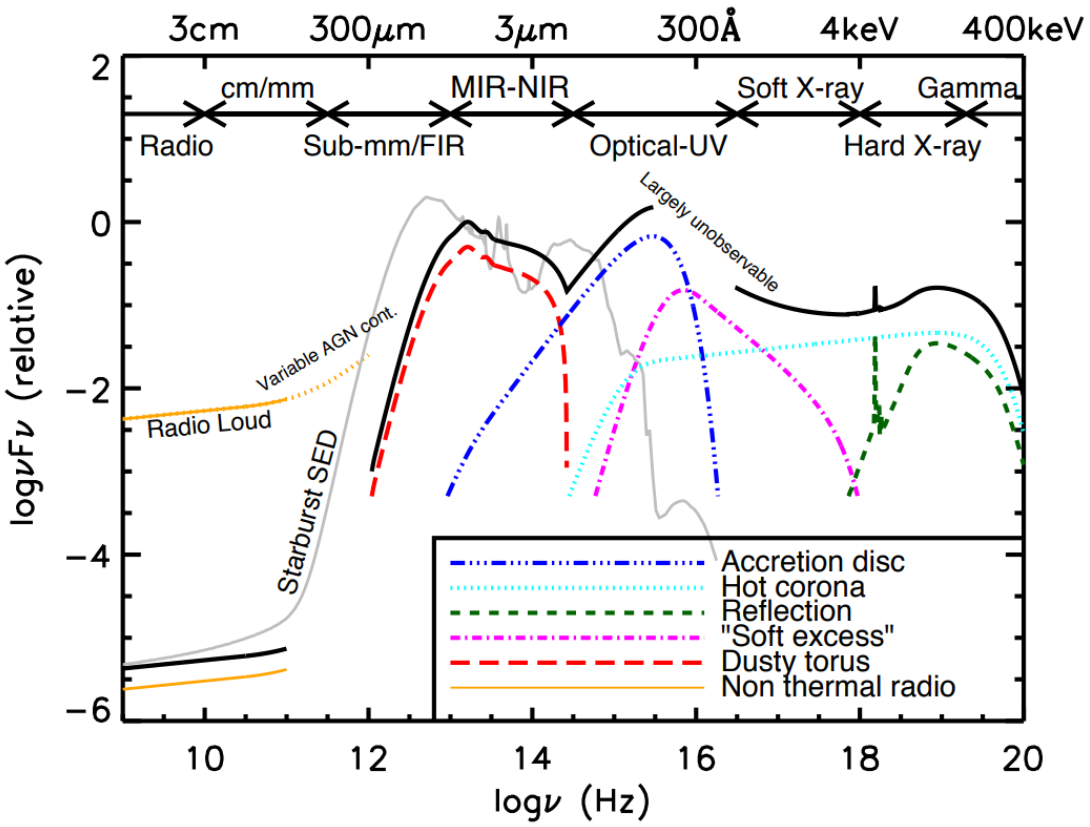

Figure 1.6: Schematic representation of the spectral energy distribution (SED) of an unobscured AGN. The black solid line represent the total SED, and the colored lines represent the different physical components. The light gray curve is the SED of a star forming galaxy for comparison. Figure from Harrison (2014).

1.1.5 Feedback

Feedback mechanisms are a critical component of galaxy evolution (Hopkins et al. (2014)). With feedback we generally refer to the combination of the effects of an input of energy from AGNs and star formation on the surrounding gas. This in turn can affect negatively (or positively) the ability of this gas to feed the new star formation and AGN activity. For this reason we call this mechanism "feedback". Feedback processes are needed to explain the discrepancy between theory and observations both for low-mass galaxies, and the observed exponential suppression of massive galaxies (Bower et al. (2012)). Simulations tend to form many more massive star forming galaxies at $z \sim 0$ than we observe, and observations indicate that most massive galaxies at $z \sim 0$ have had their star formation suppressed very rapidly. In the absence of feedback, we would also expect a larger number of small galaxies.

Outflows are one of the most evident manifestations of feedback (Cazzoli (2017)). They regulate star formation (SF) and AGN activity, and redistribute gas and dust

over large scales into the interstellar medium (ISM) and even the IGM (Aguirre et al. (2001)). It has also been proposed that outflows themselves can undergo vigorous SF (Zubovas et al. (2013)). In observation, the main driving force behind the outflows, whether it is AGN-driven or starburst-driven, is however difficult to distinguish, since several processes are often occurring at the same time.

Stellar Feedback

Star formation activity transports energy and momentum to its surroundings, which can impact the entire galaxy and affect its star forming capability (Hopkins et al. (2012)). This is observed by e.g. outflows of ionized, neutral and molecular gas, shocks and metal enrichment in the IGM. The two main scenarios for stellar driven feedback are the energy-driven and the momentum-driven scenario. In the energy-driven scenario, it is the kinetic energy released by supernovae and stellar winds that play the dominant role of counteracting and self-regulating star formation (Veilleux et al. (2005)). If the coupling between the energy injected and the surrounding ISM is efficient enough, it can drive strong and large scale outflows. This scenario is more important in low mass galaxies with a small dark matter halo, as gas can easier escape from a shallow gravitational well (Davé et al. (2011)). In the momentum-driven scenario, it is the momentum transferred by UV-radiation of young and massive stars to dust and the momentum from supernovae that are the dominating factors. This mechanism requires large optical depths to IR radiation (Davé et al. (2011)) and coupling of gas and dust in the outflow, and are therefore most effective in dusty star-forming galaxies (Murray et al. (2005)).

AGN Feedback

Stellar feedback can account for many galaxy properties, but it is not sufficient to account for the quenching of star formation in massive galaxies (Hopkins et al. (2014)). AGNs, however, can generate large and powerful outflows that can explain this. We differ between two types of AGN feedback mechanisms: the radio-mode and the quasar-mode.

The radio-mode feedback is associated with a low accretion rate to the SMBH, and radio jets injecting energy to the ISM and intracluster medium (for massive radio galaxies at the center of clusters) (Fabian (2012)). This in return keeps the surrounding gas hot, which suppresses the star formation. This mechanism dominates at late times and in massive objects in rich environments, and can explain the suppression of star formation in the central galaxies of clusters and in very massive objects (Croton et al. (2006)). The quasar mode results from short and efficient episodes of gas accretion onto the SMBH (Menci et al. (2008)). The energy released during such episodes can generate powerful outflows and expel gas from the host galaxy. This process requires large amounts of gas and can be triggered by mergers or disk instabilities.

Studying the interplay between gas involved in galactic winds in different phases can provide key information about the AGN feedback mechanism (Cicone et al. (2018a)).

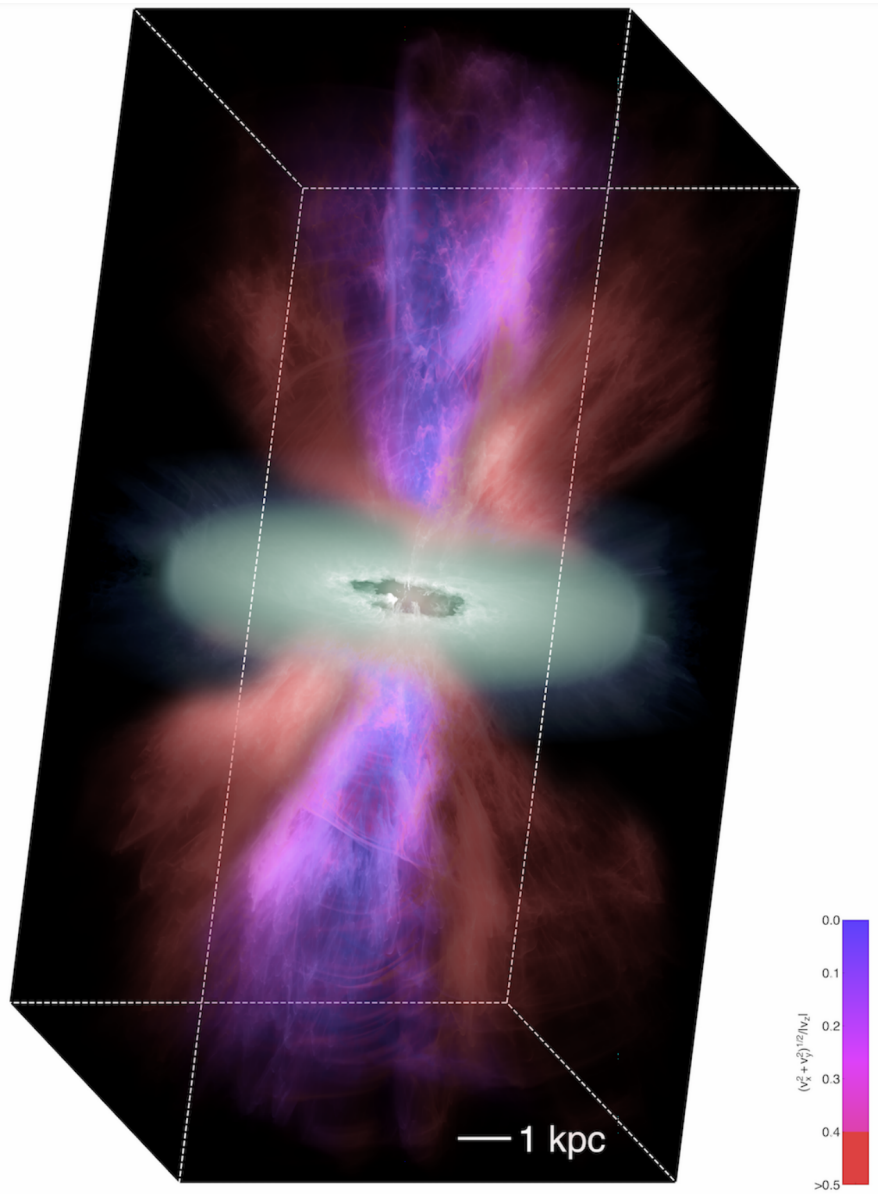

Figure 1.7: Simulation of galactic winds in a starburst system. Shown is the velocity structure of a simulated galaxy outflow. The rotating disk is shown in green. The color bar shows the logarithmic intensity of the velocity field of the gas, normalized to the total z-velocity. Figure from Schneider et al. (2018).

Galactic outflows are observed to entrain gas in multiple phases, the same phases that we observe in the normal (non-outflowing) ISM. We therefore need multiphase tracers to fully understand outflows.

One way to trace the molecular (H_2) gas, which may constitute a large fraction of the gas content in outflows, is through observations of the CO or OH emission lines (as H_2 is very challenging to detect). There are however some possibly large uncertainties on the mass estimates based only on CO or OH, so utilizing additional multiphase tracers (such as atomic neutral carbon [CI](1-0)) to measure the H_2 mass is a recommended approach (Cicone et al. (2018a)).

Recent studies combining the CO and CI line emissions in outflows (e.g Feruglio et al. (2013a), Feruglio et al. (2013b) and Cicone et al. (2018b)) have given greater insight to the mechanisms that drive feedback in nearby galaxies. A particularly interesting class of galaxies to study in this regard ULIRGs, as they show the most conspicuous cases for outflows in the nearby Universe (Arribas et al. (2014)). They also share some structural and kinematic properties with these distant galaxies. ULIRGs are therefore ideal to study outflows in environments similar to those at high redshift, but with high signal to noise and spatial resolution.

1.2 Ultra Luminous Infrared Galaxies

The first observations of galaxies in the infrared were conducted in the sixties and early seventies (Low and Kleinmann (1968), Kleinmann and Low (1970)). The new galaxy class Ultra Luminous Infrared Galaxies was however first introduced in 1984 with the all-sky survey in the mid- and far-infrared (IR) with IRAS (Soifer et al. (1984)). ULIRGs are some of the most luminous objects in the local Universe, and emit the bulk of their energy in the IR ($L_{IR} \geq 10^{12} L_o$) (Sanders et al. (2003)). The strong IR emission is due to the absorption of optical and UV radiation by dust grains which reradiate in the IR. The dust grains are heated by either extreme starburst activity, AGNs, or a combination of both (Yuan et al. (2010)).

Following IRAS in 1984, several surveys were carried out in various portions of the sky and at wavelengths covering the IR, mm, and radio bands (e.g with the Infrared Space Observatory ISO (Dole et al. (1999), Rowan-Robinson et al. (1999)), the Sub-millimeter Common-User Bolometer Array SCUBA (Smail et al. (1997)), the space telescope Spitzer (Lonsdale et al. (2004)), AKARI (Murakami et al. (2007)), Herschel Space Observatory(Eales et al. (2010)) and the Wide-field Infrared Survey Explorer WISE (Wright et al. (2010))). These have contributed to understand the physics of ULIRGs and led to the discovery of ULIRGs at high z.

ULIRGs correspond to exceptionally star forming galaxies in the local Universe, and lie above the MS of star forming galaxies as starburst galaxies. But as the MS is shifted to higher SFR at higher redshifts (see section 1.1.2), the regime of IR-luminous galaxies starts to coincide with the normal MS galaxies at high z. Hence, ULIRGs are more common at higher redshifts (early times) and more representative of the high-z SF galaxy population (Kilerci Eser et al. (2014)).

The intense IR luminosity in local ULIRGs is mainly triggered by major mergers (Pereira-Santaella et al. (2015)). The contribution of AGNs to the IR luminosity is debated, but studies of ULIRG samples indicate that the power source for the lower luminosity ones is extended starbursts, while AGNs contribute more to the bolometric luminosity in more luminous sources. Even with numerous studies at multiple wavelengths, it is still difficult to determine the relative contribution of starburst and AGN activity in individual galaxies.

Each region of the electromagnetic spectrum provides information about the components that constitute a galaxy and their physical properties. Stars, dust, and gas are constantly interacting with each other and modifying the stellar content and interstellar medium. This process is imprinted on the galaxy's spectral energy distribution (SED). Observations at multiple wavelengths and the study of the SEDs of galaxies are therefore necessary to understand galaxy formation and evolution.

1.2.1 The Spectral Energy Distribution (SED) of ULIRGs

One way to understand and extract information from the SEDs of ULIRGs is to use fitting codes, such as MAGPHYS (Cunha et al. (2015)), LePhare (Ilbert et al. (2006)), CIGALE (Boquien et al. (2019)) and MICHI2 (Liu et al. (2021)). Such codes combine multiple SED components to make a best fit to observations. A basic principle in these codes is energy conservation between the absorption of UV emission and the emission emitted in the IR by dust. With the MICHI2 code, Liu et al. (2021) attempted to decompose the SED from optical to far-IR/mm wavelengths of a sample of local ULIRGs. Figure 1.8 shows an SED fit of NGC6240 and figure 1.9 shows the galaxy properties used in this fit. In this model, they used five main components: a stellar component, a mid-IR AGN, warm and cold dust, and a radio component.

The submm/mm part of the SED is a combination of dust emission, free-free emission, and synchrotron emission (Bot et al. (2010)). Thermal free-free emission originates from the hot ionized gas in HII regions, while synchrotron radiation is emitted by relativistic particles accelerated by a magnetic field, which takes place in supernova remnants or AGNs (Klein, U. et al. (2018), Harrison (2014)). The dust emission is produced by dust grains heated by star formation and AGNs in thermal equilibrium that emit as a modified black body. Dust plays a very important role in ULIRGs.

Dust Emission

In normal disk galaxies, dust re-radiates 30% of the stellar power. In ULIRGs however, this number is up to 99% (Galliano et al. (2018)). Dust is also responsible for heating of the gas in photodissociation regions (PDR) (Draine (1978)) and acts as a catalyst for numerous chemical reactions, including the formation of the most abundant molecule in the Universe, H_2 (Gould and Salpeter (1963)).

Deducing the dust properties in a galaxy is however not straightforward (Draine and Li (2007)). One has to build a model with assumptions about the mixture constitution such as chemical composition, grain structure, shape, size, and abundance, and physical

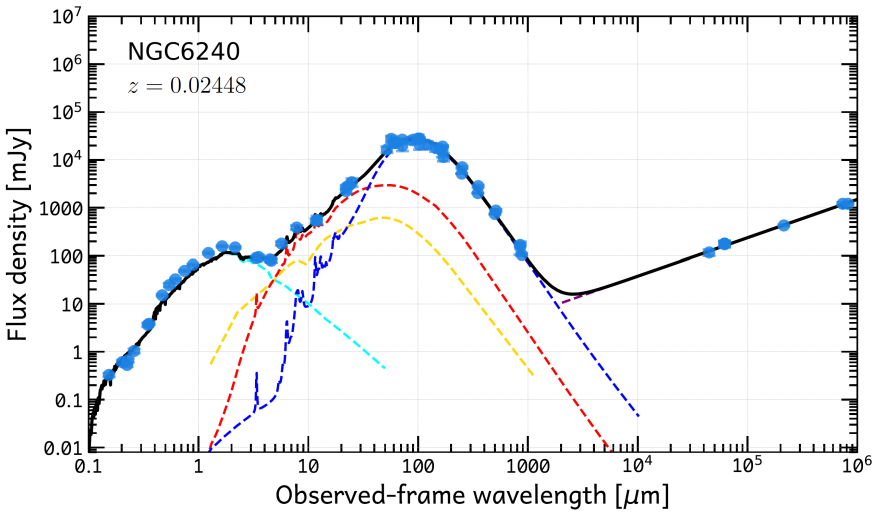

Figure 1.8: SED fit of NGC6240 obtained with the MICHI2 code. The best fit is represented with a black line, and the SED components are stellar (cyan dashed line), mid-IR AGN (yellow dashed line), warm dust (red dashed line) and cold dust (blue dashed line). The blue points are flux observations from the literature (e.g Clements et al. (2018), Chu et al. (2017), Lisenfeld et al. (2000), Iono et al. (2007)). Figure from Liu et al. (2021).

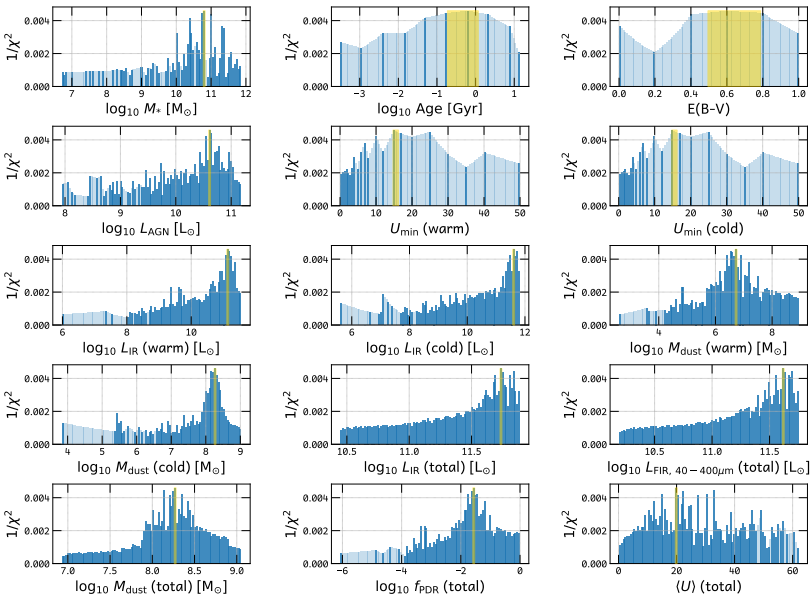

Figure 1.9: $1/\chi^2$ distributions describing the SED-fit to NGC6240. A higher $1/\chi^2$ means a better fit, and the 68% confidence level is indicated by the yellow shading. Figure from Liu et al. (2021).

conditions such as thermal excitation due to radiative or collisional heating, charging, magnetic field and grain rotation (Galliano et al. (2018)) - a virtually limitless number of ways to combine elements. This is then constrained by comparing the model predictions with observations (extinction, scattering, polarization, IR emission, and interstellar depletions).

The approach by Liu et al. (2021) in MICHI2 with warm and cold dust is based on the work by Draine and Li (2007). They calculated physical models based on probability distribution functions (PDFs) in the interstellar radiation field (ISRF). In these models, most of the dust is exposed to a minimum ambient ISRF with intensity U_{min} (cold dust), while the rest is located in a photodissociation region (PDR) ISRF with intensities from U_{min} to U_{max} (warm dust).

1.3 NGC6240

The target of this work is the merger NGC6240. NGC6240 is a local (z = 0.0245) LIRG and the result of a merger between two gas rich spiral galaxies (Feruglio et al. (2013a)). The two nuclei are located in the central region of the galaxy, separated by $\sim$ 1 kpc. Both of them host AGNs with SMBH masses exceeding $10^8 M_\odot$ (Engel, H. et al. (2010)). Due to the intense star-formation activity (Sanders and Mirabel (1996)) and the presence of tidal arms (Engel, H. et al. (2010)), it is assumed to be in the early stage of merging, between the first encounter and the final coalescence. From Hubble Space Telescope (HST) Hα images of NGC6240 (see figure 1.3), we can see a strongly disturbed butterfly-shaped morphology interpreted as evidence for a super-wind shock heating the ISM (Gerssen et al. (2004)). The Hα emission has been hypothesized to trace an outflow pattern, extending up to 10 kpc from the central region, and likely powered by both the nuclear star-formation and AGN-activity. Indeed, a molecular outflow was confirmed by Feruglio et al. (2013b), and later by Cicone et al. (2018b).

1.3.1 Extended Outflows

Feruglio et al. (2013a) presented deep observations of the CO(1-0) transition in NGC6240 obtained with the IRAM Plateau de Bure Interferometer. They found that the CO emission shows very broad and asymmetric wings detected out to velocities of -600 km/s and + 800 km/s, respectively blueshifted and redshifted of the systemic redshift. Two prominent blueshifted structures were detected in the eastward and southwestward direction, extending $\sim$ 7 kpc from the nuclear region (see figure 1.10).

The CO emission in the southwestward direction overlaps with the dust lanes interpreted as tidal tails in HST images (figure 1.3), which indicates that the gas is highly affected by galaxy interactions. The eastward emission is in the same region as the H_α filament, and supports a scenario with molecular gas compressed into a shock wave propagating eastward from the nuclei, with the AGN as the most likely driving force. High resolution observations of the CO(1-0) transition (Feruglio et al. (2013b)) strengthens this interpretation of the blueshifted emission as massive outflow, originating from the southern nucleus likely driven by both SNa winds and radiation by the

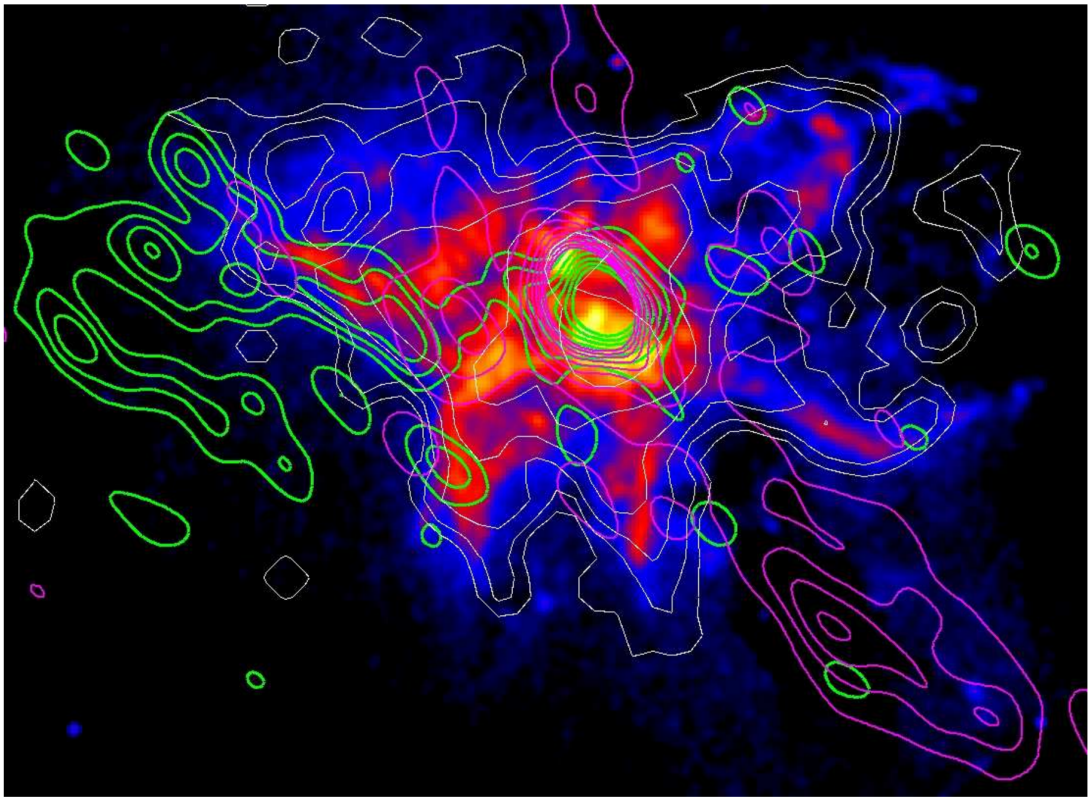

Figure 1.10: Hα map of NGC6240 with CO(1-0) emission at different velocities. -350 km/s (green contours) and -100 km/s (magneta contours). White contours are from 1.6-2 keV emission in the X-rays which traces very well the underlying Hα emission shown by the color scale. Figure from Feruglio et al. (2013a).

southern AGN. These authors found, however, that the CO emission does not peak on the southern nucleus, but rather in the midpoint between the two nuclei, a scenario not predicted by hydrodynamical simulations of mergers between gas rich galaxies (Bournaud et al. (2011)).

Cicone et al. (2018b) studied the physical properties of the massive molecular (H_2) outflows in NGC6240 with [CI](1-0) line observations from ALMA combined with ALMA CO(2-1) data and CO(1-0) data from IRAM Plateau de Bure Interferometer. As pointed out in Feruglio et al. (2013b), they found that the bulk of the outflow extends in the eastward direction. But in these observations, they also found a western outflow, aligned in the same east-west axis as the eastern component. They also concluded that both the redshifted and the blueshifted velocity components trace the same molecular outflow, based on their close spatial correspondence, as can be seen in figure 1.11.

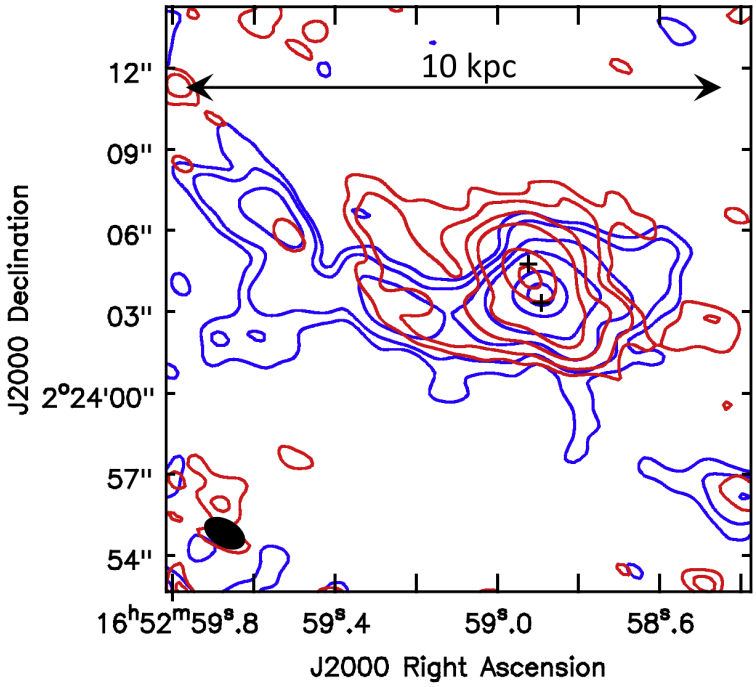

Figure 1.11: CO(2-1) blue and red wing emission in NGC6240, with positive contours starting from 5 σ. Figure from Cicone et al. (2018b).

The high resolution [CI](1-0) observations show that the redshifted emission peaks at the midpoint between the two AGNs, while the blueshifted component peaks closer to the southern nucleus, but none of them at either AGN (see figure 1.12). This separation, also detected with CO(2-1) data (Tacconi et al. (1999)), has previously been interpreted as a rotating molecular disk. This is however debated, and Cicone et al. (2018b) argues that the high CO velocity dispersion, $\sigma > 300$ km/s, suggests otherwise. The velocity field does not present the characteristic butterfly pattern of a rotating disk, and the features in the nuclear region are correlated with the high velocity wings. The high σ_v

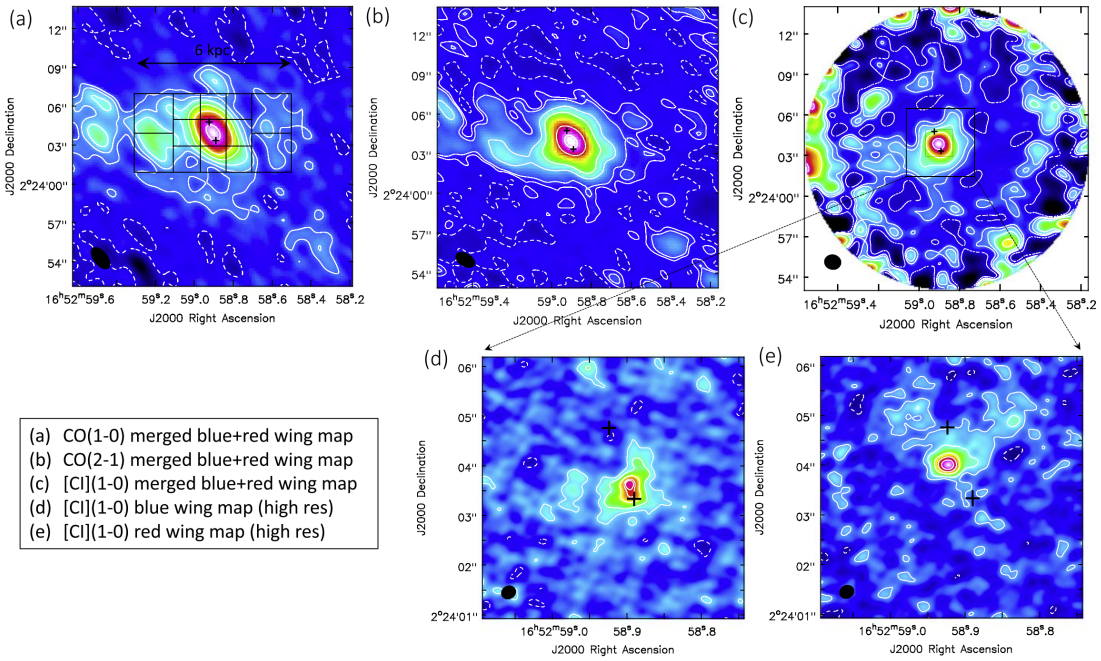

Figure 1.12: Outflow in NGC6240 observed with CO(1-0), CO(2-1) and [CI](1-0) emission. Image a-c are maps with blue and red wing combined, while d and e show the maps of the [C I](1â0) blue and red wings. Figure from Cicone et al. (2018b).

regions might rather represent places where the opening angles of the outflow widen. Therefore, Cicone et al. (2018b) concludes that the region in between the two AGNs is dominated by nuclear outflows extending in the east-west direction. The total outflow mass rate calculated is 2500 ± 1200 $M_{\odot}$ yr^{-1}. Cicone et al. (2018b) found that 60 ± 20 % of the molecular ISM belongs to the outflow, which may explain the extreme ISM of NGC6240. The CO-to-H_2 conversion factor, α_{CO}, was estimated to be higher than the optically thin value, which suggests that not all of the outflowing gas is diffuse and warm, but some may be dense. This would make star formation within this outflow more likely. Star formation in galactic outflows has also been suggested by Maiolino et al. (2017).

When galaxies collide, high velocity gas can be concentrated in the nuclear region due to gravitational torques, which causes some of the gas to lose angular momentum and flow towards the center. Gravitational torques and tidal forces can also play a part in driving gas outwards and creating tidal tails and bridges (see also section 1.1.3). According to Cicone et al. (2018b) however, the kinematics and morphology of the central region studied in that work (central 6 kpc x 3 kpc rectangular region, excluding the northern and southern parts of the galaxy, see panel a of fig 1.12) in this galaxy can hardly be explained by gravity induced mechanisms. The structures observed in the central region are correlated with features on much larger scales, and can therefore not be due to nuclear inflow. Tidal tails are not expected to be dominant in this

central 6x3 kpc^2 rectangular region studied by Cicone et al. (2018b), because of the large velocity dispersion components detected in the spectra and the overlap between highly blueshifted and highly redshifted emission which strongly suggest outflows, seen in figure 1.11. In addition, this east-west structure is consistent with the structure seen on smaller nuclear scale which points to an outflow propagating from the nuclear region out to a few kpc east-west of the two AGNs. However, tidal features may still be relevant outside this east-west outflow-dominated region.

1.3.2 Possible Driving Mechanisms of the Outflows in NGC6240

NGC6240 is one of the few sources observed hosting H_2 outflow on $\geq$ 10 kpc scales (Cicone et al. (2018b)). Based on its energetics, a purely stellar feedback mechanism can be ruled out. Instead, AGN feedback models can fully accommodate the observed outflow energetics (Faucher-Giguére and Quataert (2012), Zubovas and King (2014), Costa et al. (2014)). Several multiwavelength observations of NGC6240 also point towards a radiative-mode AGN feedback mechanism (Nims et al. (2015)). In the optical wavelengths, an ionized wind with large scale superbubbles extending tens of kpc has been observed (Yoshida et al. (2016)). This wind is in close spatial correspondence with the soft X-ray continuum, which suggests the presence of gas cooling out of a shocked medium (Nardini et al. (2013)). A diffuse component in hard X-ray continuum has been detected both in between the two AGNs (Wang et al. (2014)), located north-west of the southern nucleus - similar to the blue wing in figure 1.12 d, and in the large scale structure coinciding with both the strong NIR H_2 emission and the Hα filaments (Max et al. (2005)). Non-thermal continuum emission extending several kpc west of the AGN has been detected in radio (Colbert et al. (1994)) in an arc-like structure, with a possible eastern component (Baan et al. (2007)). There is no clear corresponding optical or NIR starlight in this region, excluding a starburst origin, and the complex morphology indicates a connection with the Hα outflow. The western component aligns with the outflow detected by Cicone et al. (2018b), and supports the theoretical association between an AGN-driven wind and extended non-thermal radiation (Nims et al. (2015)). The total radio power of these features compares to the extended radio structures observed in radio-quiet AGNs with prominent outflows (Morganti et al. (2016)).

All these observations suggest a radiative-mode AGN feedback mechanism. The launching point of the molecular outflow is however at odds with this scenario, as we would expect the multi-phase outflow to be generated in the central engine (Costa et al. (2015)). The direction of the outflow, perpendicular to the axis between the two nuclei, is also puzzling (Cicone et al. (2018b)). A complex interplay of stellar and AGN feedback processes must therefore be at work.

It is worth noting that for this source it is also difficult to determine the source of the high IR luminosity. Previous observations of the total flux in NGC6240 at IR/submm wavelengths have been conducted with telescopes with large fields of view, measuring the flux in the entire galaxy (e.g observations used in the SED fit in figure 1.8. See Liu et al. (2021) and references therein), while high resolution observations have focused mainly on the central region (e.g Tecza et al. (2008), Scoville et al. (2014), Treister

et al. (2020)). Due to the amount of gas residing in between the two nuclei, Tecza et al. (2008) and Scoville et al. (2014) suggested that most of the IR emission should be attributed to star formation processes in this region rather than the AGNs. Later higher resolution observations (0.03" with ALMA) (Treister et al. (2020)) on the other hand, concluded that most of the continuum emission detected is directly associated with the two nuclei. However, as I will show in this work, the large extent of the optical source and the dust lanes seen in figure 1.3 suggest that dust continuum may extend far beyond the nuclear region. In addition, the presence of dense gas in the outflow, making it more likely to form stars within the outflows, also gives reason to expect IR emission outside the nuclear region.

1.3.3 This Work

The focus of this thesis will be to investigate the properties of the submillimetre and millimetre continuum emission of NGC6240. I will do this by exploiting sensitive datasets acquired with ALMA. In particular, I will study the emission in regions corresponding to AGN activity (nuclear region), and outflows and tidal tails (extended region), and interpret them in the contexts of the physical mechanisms acting on such scales.

In Chapter 2 I will first describe the datasets I use in this work. I will then describe the cleaning procedure of the datasets and how I create continuum maps, before I discuss the regions where I measure the flux. In chapter 3 I will present the results and comment on the findings. In chapter 4 I will discuss the results, make hypotheses on the origins of the observed emission, and how this relates to previous observations. Finally, in chapter 5, I will present my conclusions and suggestions for future work.

Chapter 2

Observations

With the aim of investigating the cold dust emission of NGC6240, I produced several maps of the submm and mm continuum emission to inspect different regions of NGC6240. I created low resolution maps to enhance the sensitivity to extended emission and high resolution maps to look at detailed features and measure the flux from point sources. The regions used to extract the flux values are discussed later and shown in figure 2.5.

2.1 Datasets

The Atacama Large Millimeter/submillimeter Array (ALMA) is an interferometer located at 5000 m altitude in the Atacama desert in Chile. It consists of fifty-four 12m antennas with baselines up to 16 km, and twelve 7m antennas. All observations used in this work were carried out with the 12m antennas of ALMA, and cover a frequency range from 84 to 680 GHz. I used archival data, publicly available in the ALMA Science Archive. The different datasets used here are described in table 2.1. As the datasets are from different programs with different science goals, it is worth mentioning that these were not designed for measuring the continuum emission. This is important both for the data processing (as I had to look for and exclude line emission) and for the interpretation of the results, which I will come back to in section 4.2.

1. Band	2. Project code	3. Freq. Range	4. AR	5. FoV	6. Nb.ant	7. Int. time	8. Date	9. PI
3	2015.1.01439.S	84.3-100.1 GHz	0.375"	63.163"	39	30 min	2016-09-20	Saito
3	2015.1.01439.S	93.3-108.8 GHz	0.469"	57.632"	35	21 min	2016-08-23	Saito
4	2015.1.01439.S	126.2-141.7 GHz	0.441"	43.469"	39	29 min	2016-07-31	Saito
4	2015.1.01439.S	128.6-144.4 GHz	0.347"	42.657"	35	15 min	2016-08-24	Saito
6	2015.1.00003.S	221.0-240.7 GHz	0.419"	25.2"	42	4 min	2016-06-26	Saito
6	2015.1.01448.S	244.5-262.1 GHz	0.563"	22.988"	43	21 min	2016-04-16	Tunnard
6	2015.1.01448.S	238.1-255.4 GHz	0.125"	23.598"	48	221 min	2016-09.16	Tunnard
7	2013.1.00813.S	336.6-352.2 GHz	0.132"	16.907"	35	6 min	2015-05-04	Rangwala
7	2013.1.00813.S	336.6-352.2 GHz	0.558"	16.907"	35	1.5 min	2015-05-04	Rangwala
8	2015.1.00717.S	466.4-482.2 GHz	0.242"	12.277"	40	7 min	2016-05.19	Cicone
9	2015.1.00658.S	673.0-680.3 GHz	0.229"	21.814"	40	8 min	2016-03-10	Rangwala

Table 2.1: The datasets used in this work. All observations were carried out with the 12m antennas of ALMA. The first column is the wavelength band covered, the second is the project code, number 3 is the frequency range, number 4 is the angular resolution in arcsec, number 5 is the field of view in arcsec, number 6 states the number of antennas, number 7 is the integration time in minutes, number 8 is the date when the observations were conducted and number 9 is the name of the principal investigator of the project.

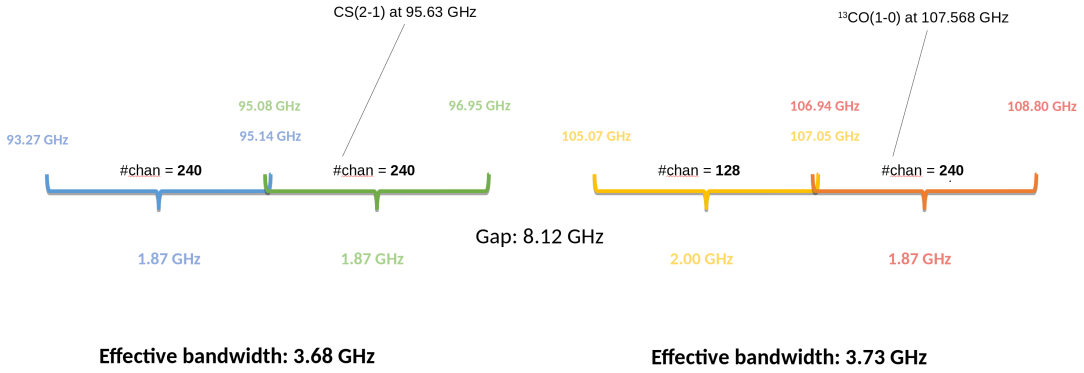

Figure 2.1: A setup of four spectral windows in band 3 covering a frequency range from 93.27-108.80 GHz. See table 2.2 for the ranges included in each of the continuum maps.

2.2 Data Processing with CASA

The datasets were processed and analyzed using the CASA software (Common Astronomy Software Application) (McMullin et al. (2007)). CASA is a suite of tools for calibration and analysis of radio astronomy data, and is the primary data processing software for ALMA. I requested calibration of the data from ALMA helpdesk, as the archival data exploited older versions of the CASA pipeline not compatible with my installation.

2.2.1 Excluding Line Emission

The focus of my analysis is continuum emission. The datasets I used were however archival data with different science goals, so in order to avoid line contamination of the continuum maps, I had to inspect all the spectral windows to look for line emission. I selected the frequency ranges with line emission at each dataset, and excluded these from the ranges I used to produce the continuum maps.

Figure 2.1 shows the setup of four spectral windows from a band 3 dataset covering the frequency range 93.27-108.80 GHz. In this dataset, the first window was line-free, the second window had emission from the CS(2-1) transition (see figure 2.2), the third window had a low number of channels (low spectral resolution) so I could not study the presence of spectral lines, and the fourth window contained line emission from CO(1-0). To avoid line contamination and get line-free datacubes, I therefore selected the frequency ranges spanned by the CS(2-1) and CO(1-0) line emissions, and excluded these from the second and fourth spectral windows. This was done with the `split` command in CASA with the continuum frequency ranges as input. For my continuum map at band 3, I used the first spectral window entirely, and the second and the fourth windows after excluding the line emission. I discarded the third spectral window (with low resolution) to be on the safe side. This process of inspecting spectral windows, selecting frequency ranges with line emission to exclude, and creating continuum maps

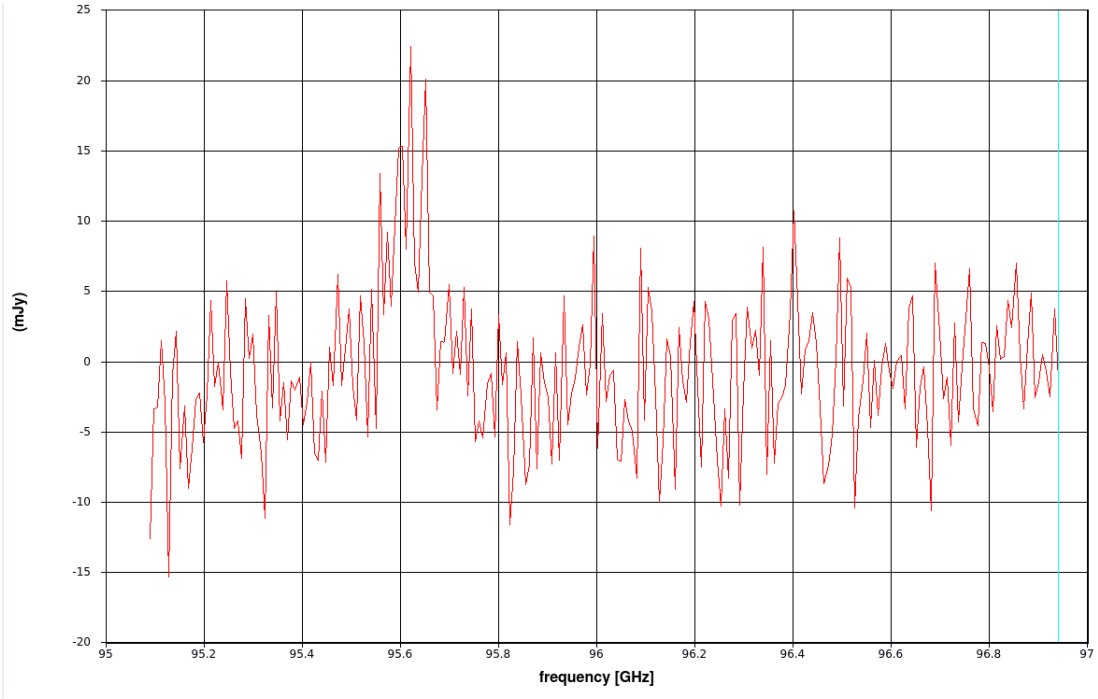

Figure 2.2: Spectral information of the second spectral window in band 3 (marked in green in figure 2.1) with 240 channels. There is a clear line at 95.6 GHz, corresponding to CS(2-1) line emission.

was repeated for all the datasets (see table 2.2 for the frequency ranges included in each spectral window). Then, to create one single collapsed continuum map for each band, I merged together the data for each of the bands.

Band	Freq. Range	Spw 0	Spw 1	Spw 2	Spw 3
3	84.3-100.1 GHz	84.29-85.10	-	96.40-97.60	98.22-98.80
		85.40-86.16		97.80-98.27	99.10-100.09
3	93.3-108.8 GHz	-	106.94-107.50	95.08-95.50	93.27â95.14 *
			107.70-108.80		
4	126.2-141.7 GHz	126.23-127.0	127.81-129.50	137.98-138.40	139.81-141.50
		127.4-128.10		138.9-139.85	
4	128.6-144.4 GHz	140.72-141.50	142.54-143.20	128.61-129.50	130.43-132.30 *
		141.70-142.59	143.70-144.40	129.8-130.48	
6	221.0-240.7 GHz	-	221.8-222.82	239.4-240.69	237.5-238.86
6	244.5-262.1 GHz	-	-	244.5-246.4 *	-
6	238.1-255.4 GHz	251.87-253.72 *	253.5-255.38 *	-	239.82-241.67 *
7	336.6-352.2 GHz	348.58-350.47 *	350.33-352.2 *	-	339.0-340.2
7	336.6-352.2 GHz	348.58-350.47 *	350.33-352.2 *	-	339.0-340.2
8	466.4-482.2 GHz	468.5-469.4	466.7-467.9	481.65-482.2	478.56-479.6
9	673.0-680.3 GHz	675.8-676.65	-	678.5-679.0	673.2-673.75
				679.4-680.2	

Table 2.2: Frequency ranges in each spectral window (spw) included in the continuum maps. When a spectral window is dominated by line emission, does not exist or when the data are affected by instrumental issues, it is denoted with a - and not used in the analysis. * means that the full range of the spectral window is included.

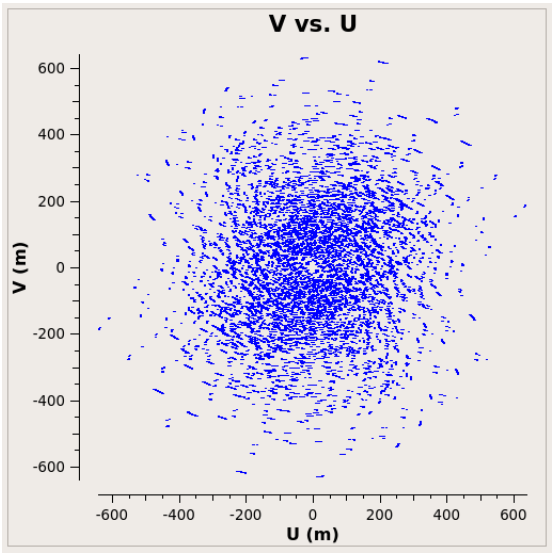

Figure 2.3: Uv coverage of band 8 data. 40 antennas were used in this observation, and the observation time was 7 minutes.

2.2.2 Cleaning Procedure

I cleaned the visibility files with the task `tclean` in CASA . Tclean is based on the CLEAN algorithm (Högbom (2003)), and is used to extract the sky brightness distribution of the source. As these are interferometric data, the uv (observation plane) coverage is never complete. The uv-plane therefore has to be filled in order to perform a Fourier transformation (see figure 2.3 for a visualization of the uv-plane in band 8). This can be done by interpolating between nearby measurements. What we then get after the Fourier transformation is a "dirty image". A dirty image is the true image convolved with the dirty beam. What the CLEAN algorithm does is reconstructing/deconvolving this image by iteratively finding the highest peak in the image, fitting the peak of the dirty beam to this peak, and subtracting the normalized dirty beam until hitting the noise level - an approach proposed by Högbom in 1974 (Högbom (1974)). Because of the high number of antennas in ALMA, the sidelobes present in the dirty image and need to be cleaned in the deconvolution operation are generally not a huge issue, unless the source has a very bright central peak.

I performed the clean algorithm with multi-frequency synthesis ('mfs' in `tclean`) to create a collapsed map, and used Briggs weighting, with the robust parameter set to 0.5. I used the standard gridding option that uses a prolate spheroidal function. The dishes that make up the telescope array are not uniformly sensitive to incoming radiation from all directions, which results in a primary beam pattern on the image, where the size of the primary beam is determined by the diameter (12m) of the antennas. The effects of this can be corrected for by dividing the deconvolved image with an average primary beam pattern. In CASA this is done with the command `pbcor`. To enhance the sensitivity to extended emission, I also created low resolution (2") maps with uv-

tapering. The effect of the tapering can be seen in figure 2.4, where the left is a high resolution continuum map of band 3, and the right image is a low resolution map with details "smoothed" out. I created one high resolution and one low resolution map of each of the bands used in this work (band 3, 4, 6, 7, 8, and 9).

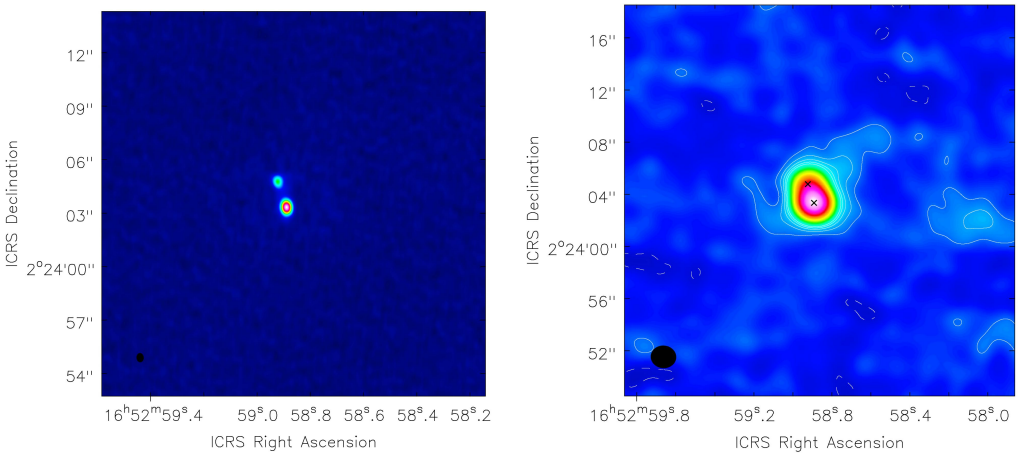

Figure 2.4: A visualization of the tapering effect on the continuum maps. Left: High resolution image of the continuum emission observed in band 3. Right: The continuum map with uv-tapering applied, which lowers the resolution (see the bigger synthesized beam size in the bottom left) and so enhances the sensitivity to extended areas. The two AGNs in NGC6240 are marked in the uv-tapered image as black crosses, with locations from Hagiwara et al. (2011).

2.2.3 Flux Measurements

Figure (2.5) shows the two regions in which I measured the fluxes. The small box covers the nuclear region with the two AGNs (1.5 kpc x 1.5 kpc) and the large box encompasses an extended region not including the small box (4.1 kpc x 3.3 kpc), both centered around RA = 16:52:58.892 and Dec = +02.04.03.858. In the high resolution maps, I used five boxes in total with the same size as the beam size (0.26 kpc x 0.26 kpc), covering the southern and northern nucleus, in addition to three additional point sources detected in this work (see coordinates in table 3.1).

Before settling on the final choice of boxes shown in figure 2.5, several attempts were made to identify the optimal boxes that allowed me to sample the nuclear region and maximize the coverage of extra-nuclear emission. A larger box would in theory include more extended emission, and multiple boxes in different areas could provide information about the continuum emission related to different processes. The attempts of using more than two boxes resulted however in very low signal to noise ratios (S/N) in many of the boxes at higher frequency bands (where the sensitivity to extended emission decreases). Increasing the box size also resulted in a low S/N. The resulting two boxes are therefore a compromise between achieving a high S/N in most of the bands and trying to capture

the extended emission. I therefore decided that the boxes shown in figure 2.5 were the optimal ones with the available data.

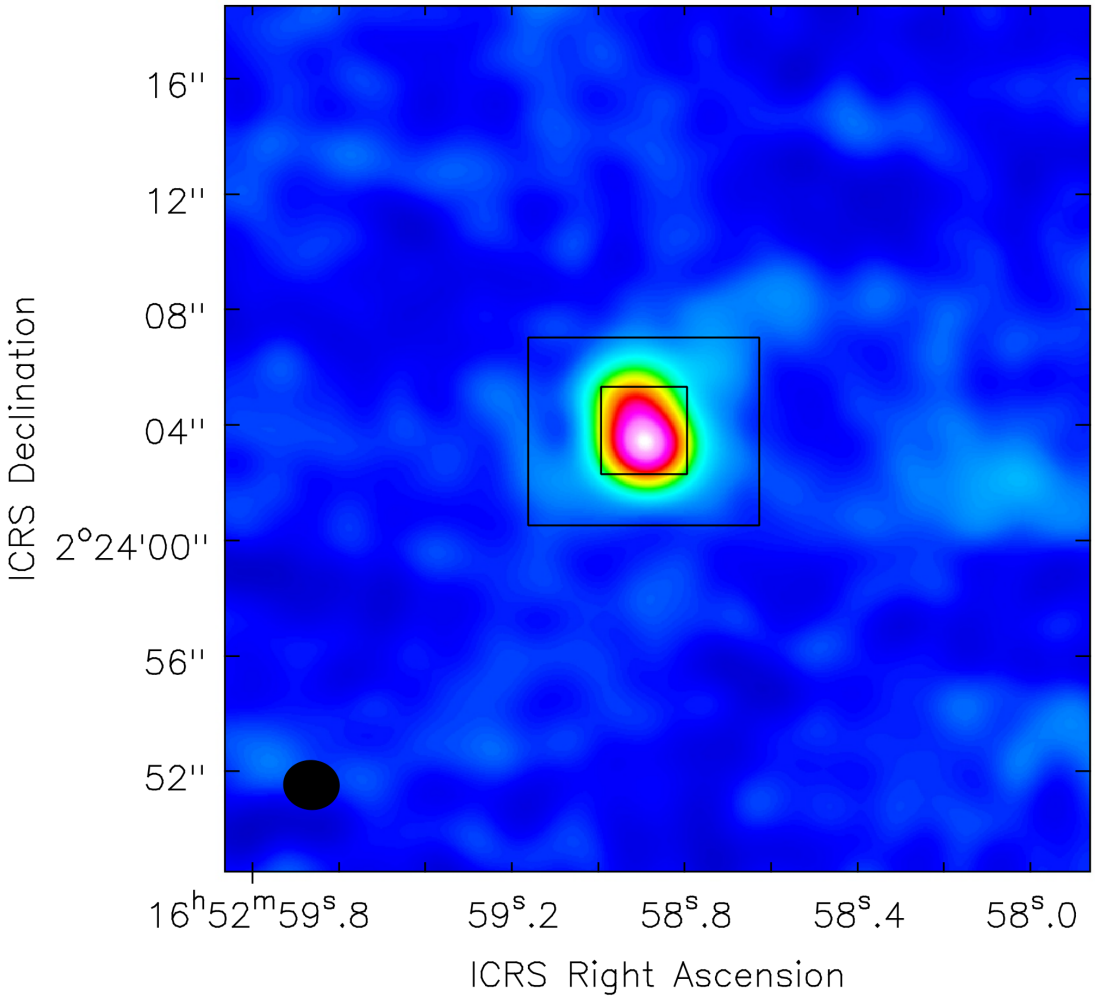

Figure 2.5: Cleaned map of band 3 emission, with uv-tapering applied. The two boxes are the collecting areas, where the flux in the small box is subtracted from the total flux in the large box. Size of large box: 8" x 6.5" (4.1 kpc x 3.3 kpc). Size of small box: 3" x 3" (1.5 x 1.5 kpc). Here I see a clear extended band 3 emission outside the large box, but as no significant counterpart is detected in the other bands, I decided to use this box in order to attain a high S/N in most of the bands.

Chapter 3

Results

I have divided this chapter into two subsections. In the first section, I present the results from the low resolution maps, with comments on the shape of the emission and the flux measurements. In the second section, I present results from the high resolution maps, with focus on the new point sources detected in this work.

3.1 Nuclear and Extended Emission

The flux measurements in the central and extended region are listed in table 3.2, and the low resolution continuum maps are shown in figures 3.3 (band 3 and band 4), 3.4 (band 6 and band 7) and 3.5 (band 8 and band 9). A high signal to noise ratio (S/N $\geq$ 9) is achieved in the central box for all bands. The S/N in the extended box is $\geq$ 2.8 for band 3 to 7. The noise level of the outer box in band 8 and 9 is however very high, and I will use upper limits when referring to these datapoints in the discussion.

The total flux observed in the nuclear area is lowest in band 3 and 4, $F_\nu = 8.8 \pm 0.14$ mJy and $F_\nu = 7.8 \pm 0.15$ mJy respectively. It increases for higher frequencies, and is almost two orders of magnitude larger in band 9, with $F_\nu = 170 \pm 13$ mJy. This is in accordance with the modeled SED of NGC6250 (figure 1.8) in section 1.2.1. An interesting observation is that the peak of the continuum emission is closer to the southern AGN than the northern in all bands. I will look more into this when inspecting the high resolution maps.

The main result from the low resolution maps is the detection of a significant extended emission, observed at all bands. In band 3 to 7, the extended region accounts for up to 32 percent of the total measured flux. The implications from this result will be discussed in section 4.2.

When studying the shape of the emission in each of the low resolution maps, I see several notable features. Starting with band 3 (figure 3.3, left panel), I detect two wing-like features extending in the northeast and the southeast direction. These features are however not visible in band 4 or higher frequencies, so the origin could be synchrotron or free free emission which rise at lower frequencies - although with only one data point, it is hard to constrain. There is also a significant amount of emission detected $\sim$6.5

Source	RA	Dec
AGN-N	16:52:58.9240	02.24.04.776
AGN-S	16:52:58.8902	02.24.03.350
C-11	16:52:59.256	02.24.11.458
C-4	16:52:58.9224	02.24.04.0158
C-3	16:52:58.895	02.24.03.664
R1	16:52:58.8885	02.24.03.326
R2	16:52:58.8993	02.24.03.602
Blue wing	16:52:58.8946	02.24.03.52
Red wing	16:52:58.9224	02.24.04.0158

Table 3.1: Position of sources referred to in this work. AGN positions and radio sources R1 and R2 are based on VLBI radio observations Hagiwara et al. (2011). Blue wing and red wing are from Cicone et al. (2018b).

.

kpc west of the nuclear region. In band 4 (figure 3.3, right panel), there is a significant amount of emission detected northeast of the nuclear region, at $\sim$ 4.3 kpc from the northern nucleus. This emission is even more apparent in band 6 (figure 3.4, left panel). I will refer to this source as C-11 (where 11 indicates the approximate declination). In band 6 there is also emission extending northwards, in a pattern turning east towards C-11. C-11 is also evident in band 7 (figure 3.4, right panel). Here there are also two wings in the same southeast direction as in band 3. C-11 is outside the field of view in band 8 and 9 (figure 3.5). The emission northwards in band 8 follows the same pattern as in band 6. In band 9 there is some extended emission aligned in the east-west direction. These features will be discussed in section 4.1.

3.2 High Resolution Maps

Figure 3.6 to 3.11 are high resolution images of the continuum emission with the two AGNs (from now referred to as AGN-N and AGN-S) marked as black crosses. The fluxes from these in addition to C-11 are listed in table 3.3, and their positions in table 3.1.

For band 3, 4, and 6, most of the emission is centered around each nucleus. This is expected from previous studies of the continuum emission (Treister et al. (2020)). Band 7 has a surprisingly faint emission around the northern AGN, and most of the flux is centered in the southern part of the nuclear region. The emission in band 8 and 9 is even more conspicuous, with a clear offset between the peaks of the continuum and the two AGNs.

There are two peaks that stand out in band 9. One is located northeast of the southern nucleus and will be referred to as C-4. The other is closer to the southern nucleus, and has a clear counterpart in band 8. I will refer to this point as C-3 (positions of C-3 and C-4 are listed in table 3.1 and in map 3.2). In figure 3.12 I have added

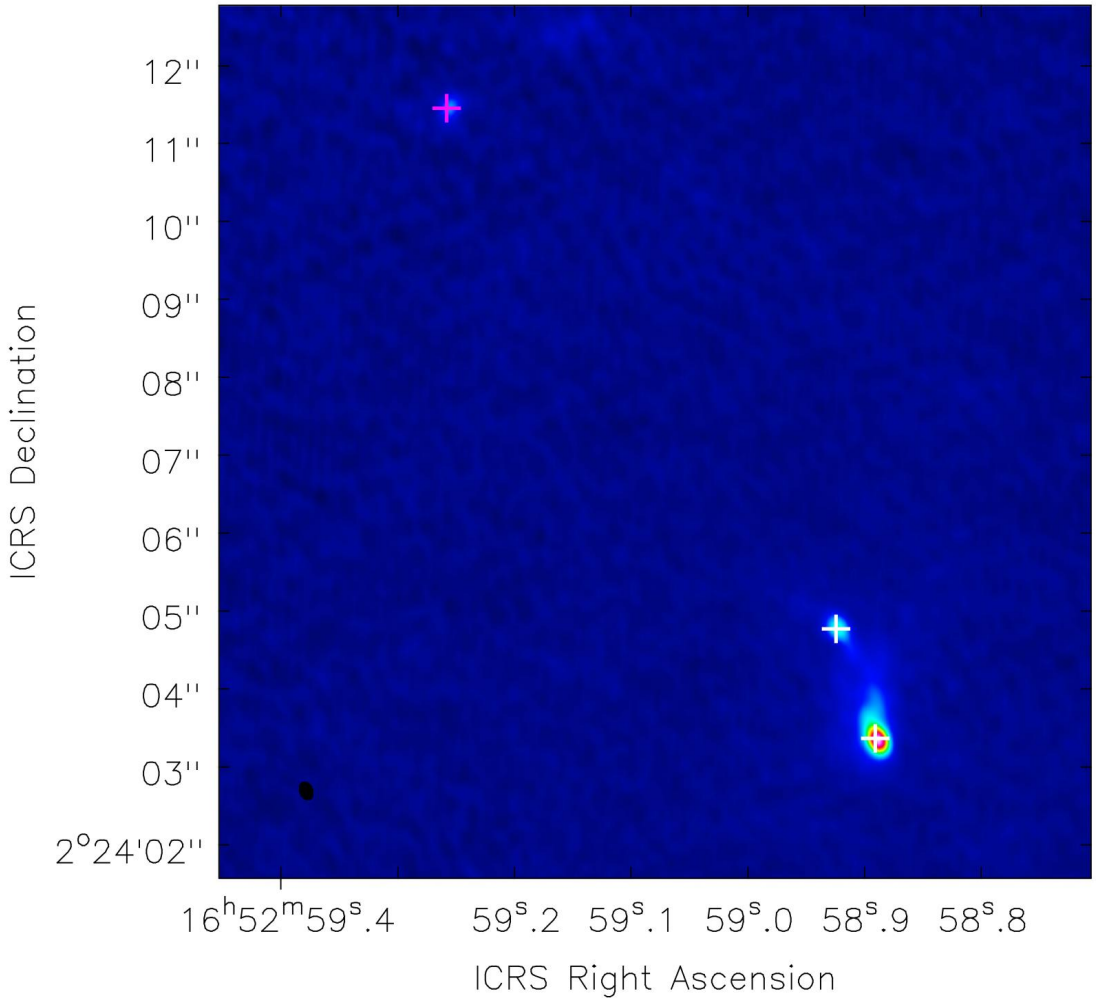

Figure 3.1: Position of C-11 marked as a magenta cross in addition to the two AGNs marked as white crosses (positions from Hagiwara et al. (2011)).

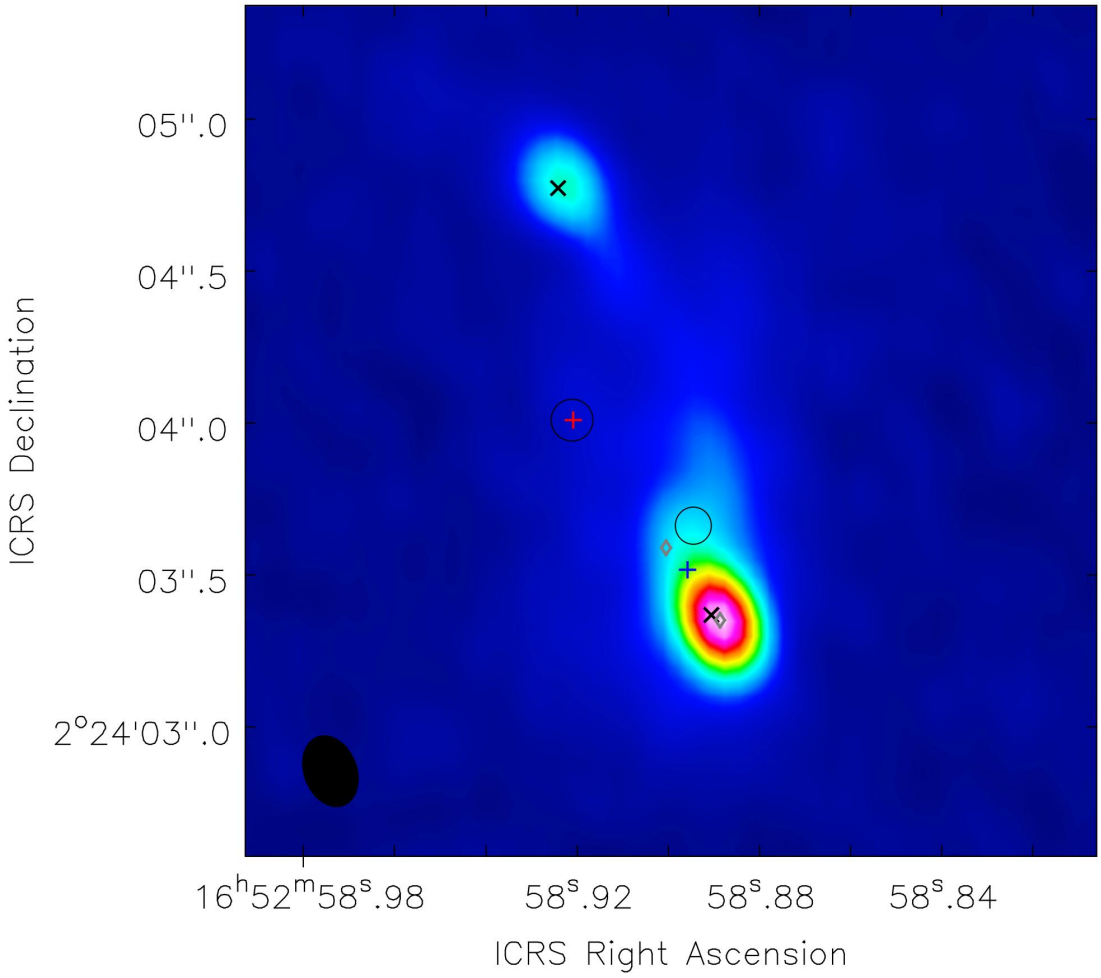

Figure 3.2: Positions of the central sources referenced in this work in band 6. AGNs are marked as black crosses (positions from Hagiwara et al. (2011)), red and blue wing peaks from [CI] observations marked as red and blue crosses (from Cicone et al. (2018b)), and VLBI radio sources as gray diamonds (Hagiwara et al. (2011)). C-3 and C-4 are marked as black circles, where C-3 is closest to the southern AGN.

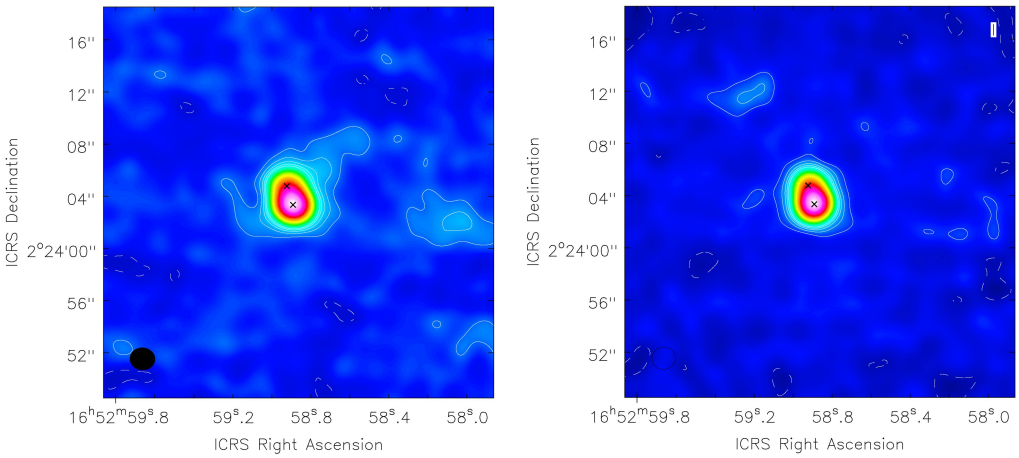

Figure 3.3: Low resolution images of the continuum emission observed at submm/mm wavelengths. Contours correspond to: (-4σ, -2σ, 2σ, 4σ, 6σ, 8σ, 10σ). The synthesized beams are shown at the bottom-left of each map. The two AGNs are marked as black crosses, with positions based on VLBI radio observations Hagiwara et al. (2011). Left: Emission band 3 (average frequency $\sim$ 97 GHz. There is a clear extension of the emission in the north-west and east/southeast, in addition to a significant amount of emission offset by a few arcsec to the west. Right: Emission from band 4 (average frequency $\sim$ 130 GHz). A peculiar point source, which I denote C-11, emerges in the northeast and will be studied in greater detail in section 3.2 in the high resolution maps.

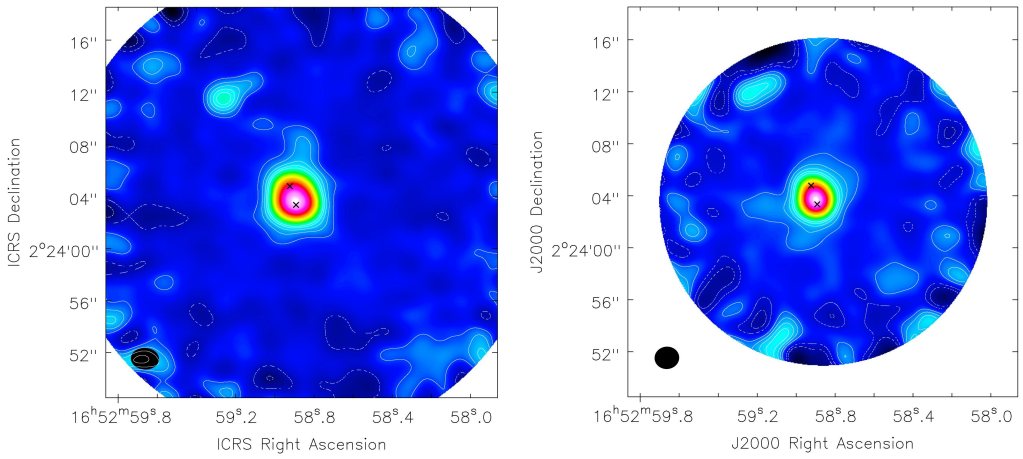

Figure 3.4: Low resolution images of the continuum emission observed at submm/mm wavelengths. Contours correspond to: (-4σ, -2σ, 2σ, 4σ, 6σ, 8σ, 10σ). The synthesized beams are shown at the bottom-left of each map. The two AGNs are marked as black crosses, with positions based on VLBI radio observations Hagiwara et al. (2011). Left: Emission from band 6 (average frequency $\sim$ 240 GHz). C-11 is even more apparent here, associated with a pattern stretching northwards from the nuclear region. Right: Emission from band 7 (average frequency $\sim$ 355 GHz). The emission from C-11 is also apparent in this band. Here I also detect some emission in the southeast direction.

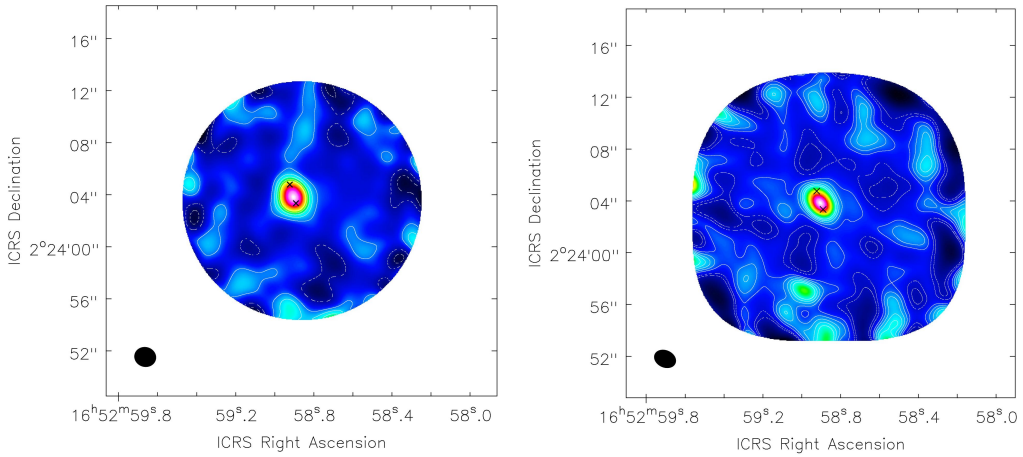

Figure 3.5: Low resolution images of the continuum emission observed at submm/mm wavelengths. Contours correspond to: (-4σ, -2σ, 2σ, 4σ, 6σ, 8σ, 10σ). The synthesized beams are shown at the bottom-left of each map. The two AGNs are marked as black crosses, with positions based on VLBI radio observations Hagiwara et al. (2011). Left: Emission from band 8 (average frequency $\sim$ 474 GHz). An extension of the emission northwards is spatially correlated with the northward emission in band 6. Right: Emission from band 9 (average frequency $\sim$ 676 GHz), with extensions aligned in the east-west direction.

Box	Large Box	Small Box
BAND3 $\nu = 97$ GHz $+ \Delta\nu_1$		
F_ν [mJy/beam]	0.34 ± 0.059	3.6 ± 0.059
F_ν [mJy]	3.8 ± 0.68	8.8 ± 0.14
S/N	5.7	60
BAND4 $\nu = 130$ GHz $+ \Delta\nu_2$		
F_ν [mJy/beam]	0.23 ± 0.057	3.0 ± 0.057
F_ν [mJy]	2.8 ± 0.70	7.8 ± 0.15
S/N	4.0	52
BAND6 $\nu = 240$ GHz $+ \Delta\nu_3$		
F_ν [mJy/beam]	0.48 ± 0.10	4.9 ± 0.10
F_ν [mJy]	5.2 ± 1.1	11.6 ± 0.23
S/N	4.7	48
BAND7 $\nu = 355$ GHz $+ \Delta\nu_4$		
F_ν [mJy/beam]	1.2 ± 0.44	11.4 ± 0.44
F_ν [mJy]	14.4 ± 5.2	30 ± 1.1
S/N	2.8	26
BAND8 (12m)$\nu = 474$ GHz $+ \Delta\nu_5$		
F_ν [mJy/beam]	0.77 ± 3.2	29 ± 3.2
F_ν [mJy]	12 ± 48	96 ± 10
S/N	0.25	9.3
BAND9 $\nu = 676$ GHz $+ \Delta\nu_6$		
F_ν [mJy/beam]	0.068 ± 3.8	47 ± 3.8
F_ν [mJy]	1.5 ± 83	170 ± 13
S/N	0.018	12

Table 3.2: Flux measured in the central area (1.5 kpc x 1.5 kpc) and extended area(4.1 kpc x 3.3 kpc). $\Delta\nu$-values are as follows: $\Delta\nu_1 = 12$ GHz, $\Delta\nu_2 = 9.1$ GHz, $\Delta\nu_3 = 21$ GHz, $\Delta\nu_4 = 7.8$ GHz, $\Delta\nu_5 = 7.9$ GHz and $\Delta\nu_6 = 3.6$ GHz.

Box	AGN-S	AGN-N	C-11	C-4	C-3
BAND3 $\nu = 97$ GHz + $\Delta\nu_1$					
F_ν [mJy/beam]	3.0 ± 0.026	0.94 ± 0.026	0.0063 ± 0.026	0.25±0.026	0.30±0.026
F_ν [mJy]	4.0 ± 0.029	1.3 ± 0.029	0.0084 ± 0.029	0.33±0.029	0.41±0.029
S/N	116	36	0.24	9.6	12
BAND4 $\nu = 130$ GHz + $\Delta\nu_2$					
F_ν [mJy/beam]	2.8 ± 0.021	0.81 ± 0.021	0.096 ± 0.021	0.18±0.021	0.27±0.021
F_ν [mJy]	3.3 ± 0.020	0.94 ± 0.020	0.11 ± 0.020	0.21±0.020	0.32±0.020
S/N	137	39	4.7	9	13
BAND6 $\nu = 240$ GHz + $\Delta\nu_3$					
F_ν [mJy/beam]	0.87 ± 0.020	0.29 ± 0.020	0.15 ± 0.020	0.17±0.020	0.15±0.020
F_ν [mJy]	5.5 ± 0.11	1.9 ± 0.11	0.97 ± 0.11	1.1±0.11	0.96±0.11
S/N	43	14	7.5	8.5	7.5
BAND7 $\nu = 344$ GHz + $\Delta\nu_4$					
F_ν [mJy/beam]	8.8 ± 0.22	3.3 ± 0.22	2.9 ± 0.22	4.4±0.22	5.2±0.22
F_ν [mJy]	5.1 ± 0.11	1.9 ± 0.11	1.7 ± 0.11	2.5±0.11	3.0±0.11
S/N	40	15	13	20	24
BAND8 $\nu = 474$ GHz + $\Delta\nu_5$					
F_ν [mJy/beam]	6.3 ± 0.83	3.0 ± 0.83	N/A	3.5±0.83	2.9±0.83
F_ν [mJy]	22 ± 2.4	11 ± 2.4	N/A	13±2.4	10±2.4
S/N	7.5	3.6	N/A	4.2	3.5
BAND9 $\nu = 676$ GHz + $\Delta\nu_6$					
F_ν [mJy/beam]	7.7 ± 1.1	1.7 ± 1.1	N/A	7.3±1.1	9.5±1.1
F_ν [mJy]	30 ± 3.7	6.5 ± 3.7	N/A	28±3.7	37±3.7
S/N	7.0	1.5	N/A	6.6	8.6

Table 3.3: Flux measured around point sources in high resolution images. Size of measurement areas is 0.26 kpc x 0.26 kpc. S/N calculated with average flux and rms values. $\Delta\nu$-values are as follows: $\Delta\nu_1 = 12$ GHz, $\Delta\nu_2 = 9.1$ GHz, $\Delta\nu_3 = 21$ GHz, $\Delta\nu_4 = 7.8$ GHz, $\Delta\nu_5 = 7.9$ GHz and $\Delta\nu_6 = 3.6$ GHz.

contours to the high resolution image of band 9 for a more visual representation of the increasing emission around the two new sources that are found in the region between the two known AGNs. I also added contours from band 3 and 6 in figure 3.13. This comparison allows me to show that the emission from the two new sources is clearly larger in the higher frequency bands. We see however already in band 6 some additional emission around C-4.

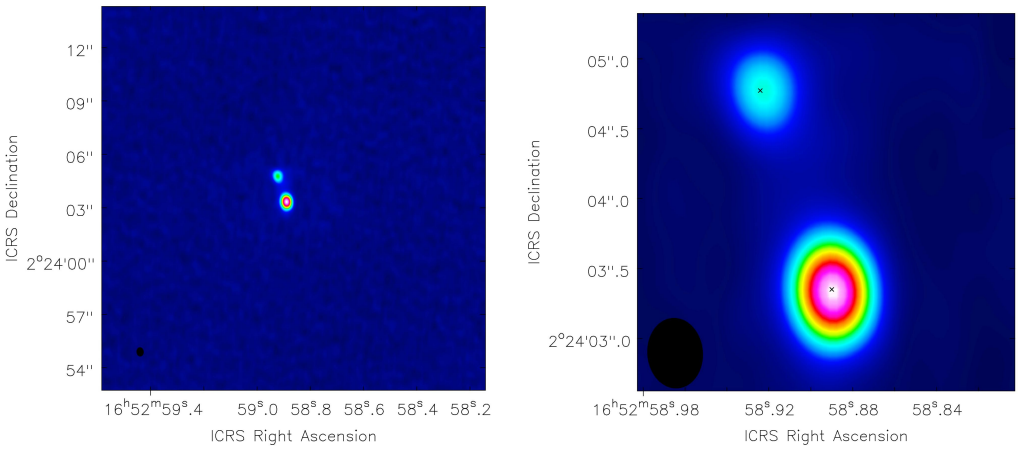

Figure 3.6: High resolution images of continuum emission observed at submm/mm wavelengths. The synthesized beams are shown at the bottom-left of each map. Left: Emission from band 3 in a region including the position of C-11. Right: Nuclear region in band 3, with the two AGNs marked as black crosses, with positions based on VLBI radio observations Hagiwara et al. (2011).

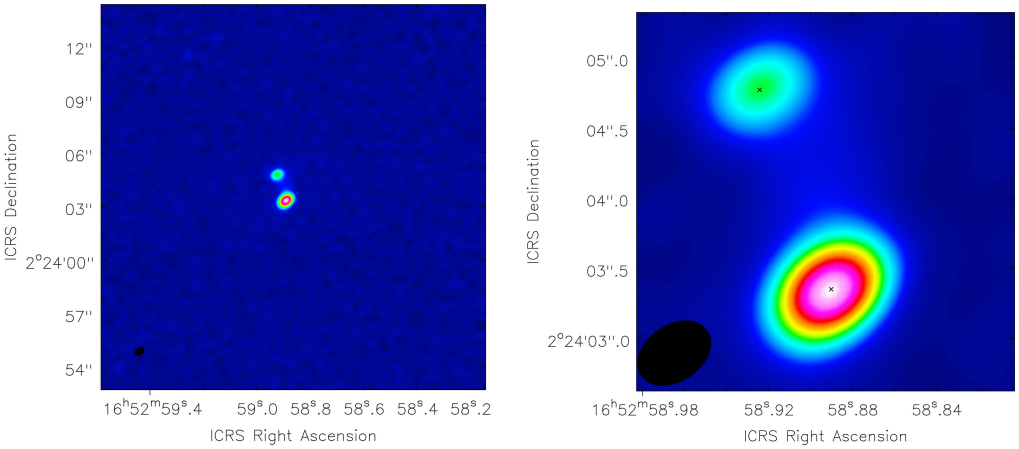

Figure 3.7: High resolution images of continuum emission observed at submm/mm wavelengths. The synthesized beams are shown at the bottom-left of each map. Left: Emission from band 4 in a region including the position of C-11. Right: Nuclear region in band 4.

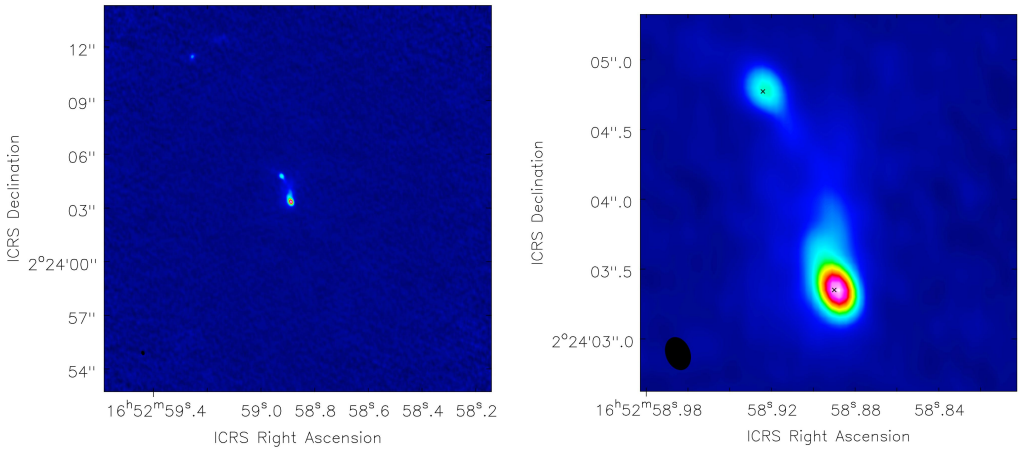

Figure 3.8: High resolution images of continuum emission observed at submm/mm wavelengths. The synthesized beams are shown at the bottom-left of each map. Left: Emission from band 6 in a region including the position of C-11. Right: Nuclear region in band 6.

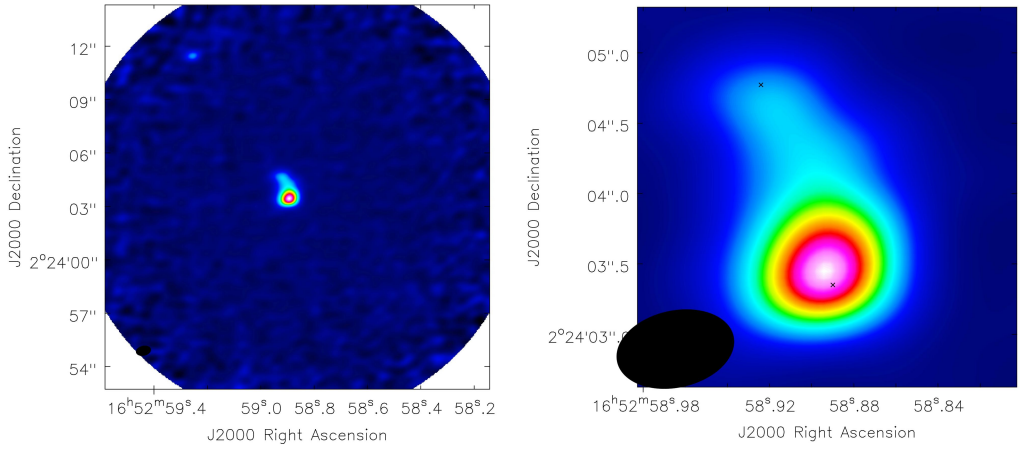

Figure 3.9: High resolution images of continuum emission observed at submm/mm wavelengths. The synthesized beams are shown at the bottom-left of each map. Left: Emission from band 7 in a region including the position of C-11. Right: Nuclear region in band 7.

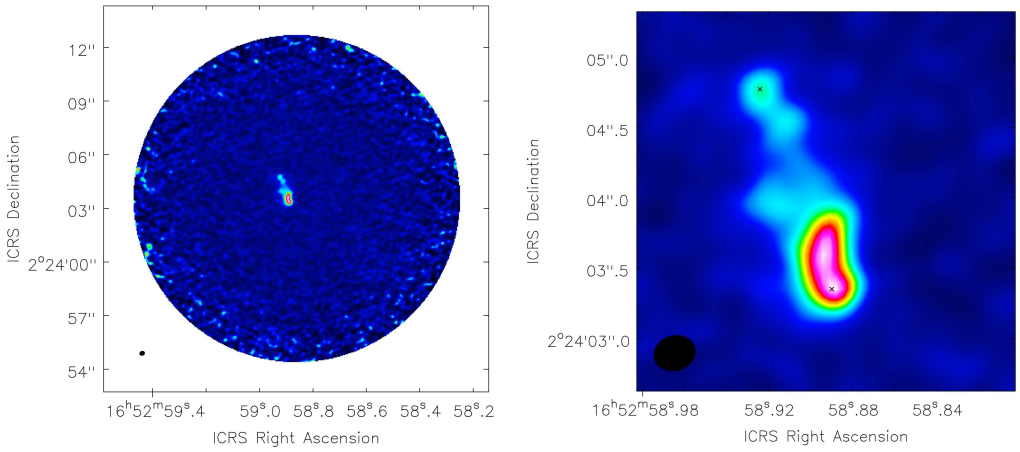

Figure 3.10: High resolution images of continuum emission observed at submm/mm wavelengths. The synthesized beams are shown at the bottom-left of each map. Left: Emission from band 8 at full size, C-11 outside the field of view. Right: Nuclear region in band 8, with the two AGNs marked as black crosses, with positions based on VLBI radio observations Hagiwara et al. (2011).

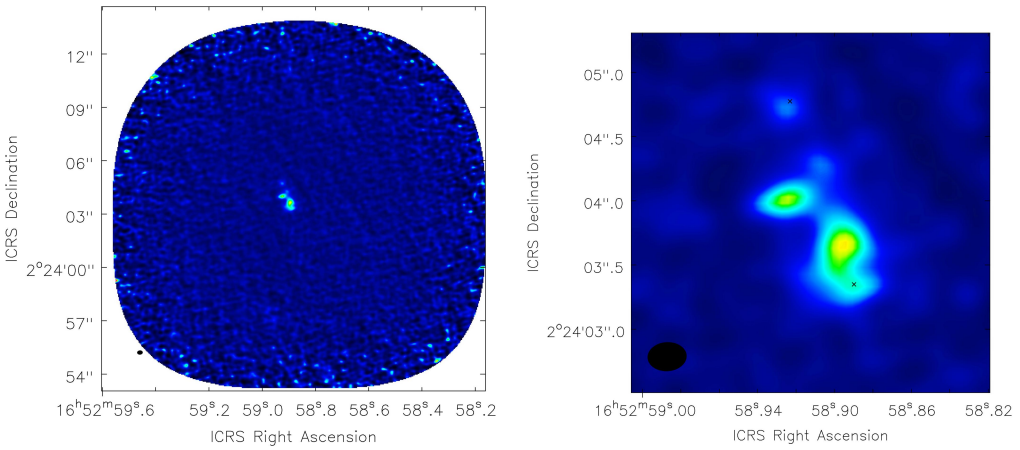

Figure 3.11: High resolution images of continuum emission observed at submm/mm wavelengths. The synthesized beams are shown at the bottom-left of each map. Left: Emission from band 9 at full size, C-11 outside the field of view. Right: Nuclear region in band 9, with the two AGNs marked as black crosses, with positions based on VLBI radio observations Hagiwara et al. (2011).

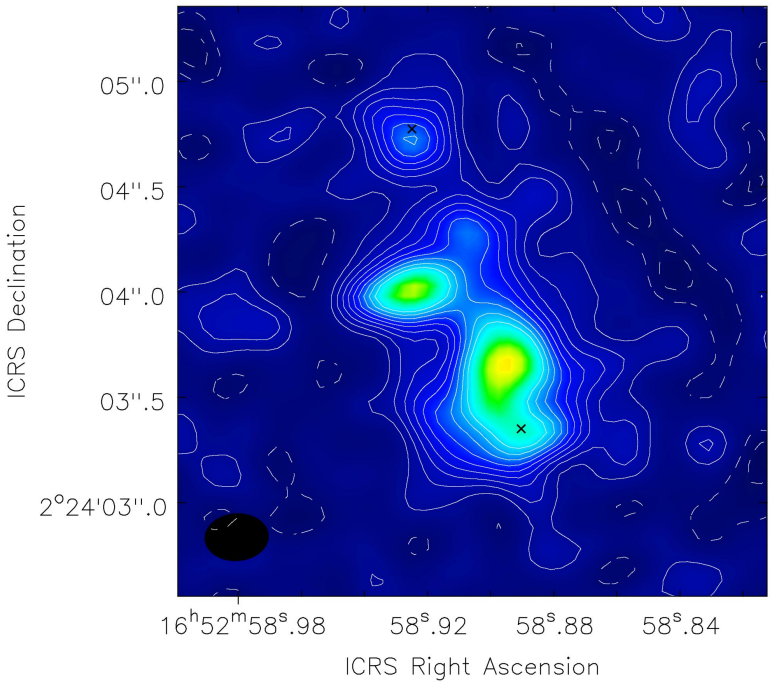

Figure 3.12: High resolution image of band 9 data with contours at (-3σ,-2σ,-1σ,1σ,2σ,3σ,4σ,5σ,6σ,7σ,8σ,9σ) and southern and northern AGN marked as black crosses (Hagiwara et al. (2011)). Position of central source is RA = 16:52:58.925, Dec = 02.24.04.018.

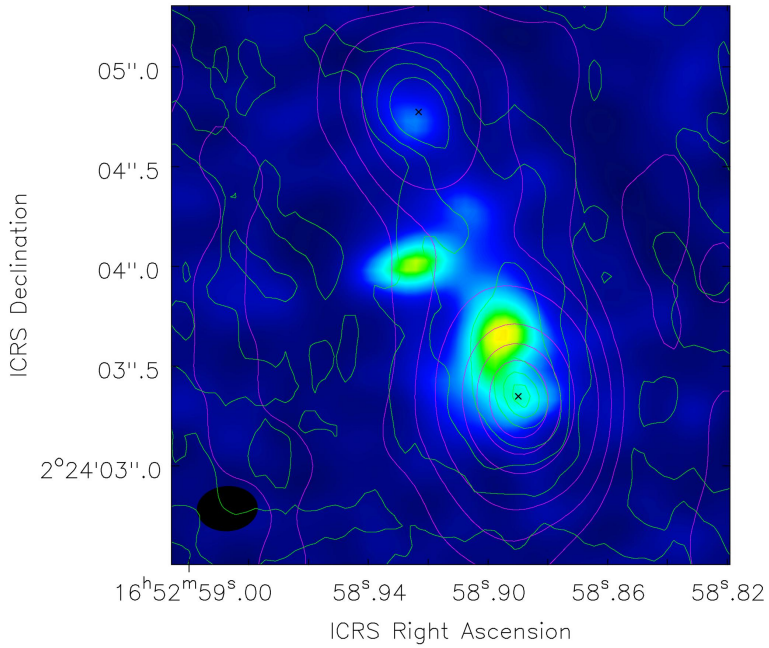

Figure 3.13: High resolution image of band 9 data with contours from band 3 (magenta) and band 6 (green) at (1σ, 5σ, 10σ, 20σ, 60σ, 100σ, 140σ). Southern and northern AGN are marked as black crosses (Hagiwara et al. (2011)). Position of central source is RA = 16:52:58.925, Dec = 02.24.04.018.

Chapter 4

Discussion

NGC6240 is a complex source with a very disturbed morphology (Treister et al. (2020)). It is therefore not straightforward to accurately describe the processes behind what we observe. The sources behind the submm/mm continuum emission might be young stars, which form in dusty molecular clouds. Molecular clouds are located primarily in the disk of spiral galaxies, but the distribution of gas and dust in the ISM during a merger is highly disturbed, and star formation might occur far away from the nuclear region, such as in outflows or tidal tails. AGN activity in the nuclear region is another possible source of submm/mm emission, and it can be more significant in highly obscured quasars, and NGC6240 hosts two of such quasars in its nucleus (Nardini et al. (2013)). As discussed in section 1.3.2, AGN feedback is probably the driving mechanism of the multi-phase outflows observed in NGC6240, which in turn may indirectly trigger star formation (Maiolino et al. (2017), Zubovas and King (2014)). Studying the dust emission in NGC6240 may therefore give insight into the interplay between AGN and star formation in major galaxy mergers.

Previous single-aperture studies have focused on the total submm/mm emission of NGC6240 (without spatial information) (e.g Wright et al. (1984), Clements et al. (2018), Chu et al. (2017), Lisenfeld et al. (2000), Iono et al. (2007)), while more recent high resolution studies have focused on emission in the nuclear region (i.e mainly the central kpc hosting the two AGNs, Scoville et al. (2014), Treister et al. (2020)). In this work, I have used sensitive interferometric observations to bridge between previous works and try to identify additional sources of continuum outside the nuclear region which may be related to outflows or tidal tails.

In the next sections I will first discuss how the continuum emission detected in this work might be related to the outflow observed by Cicone et al. (2018b). Then I will discuss my results compared with the modeled SED of NGC6240 and previous observations (figure 1.8). Lastly, I will discuss the new point sources detected in this work, and their possible origin.

4.1 Continuum Emission Associated With Outflows

By comparing the observations in this work with the CO and [CI] maps from Cicone et al. (2018b), I find that the dust emission is strongly correlated with the molecular outflow. Among the extended components, the north-west wing detected in band 3 in the low resolution map (figure 3.3) follows the outflow observed in the CO(1-0) map (figure 1.12 a). The southeast component detected both in band 3 and in band 7 is in the same region as a strong outflow detected in the CO(1-0), C(2-1), and CI(1-0) maps. The emission in band 6 in the north-east direction is also spatially correlated to the redshifted CO(2-1) emission (figure 1.11).

The detection of dust emission in the central region in between the two AGNs is however particularly interesting. In figures 4.1 and 4.2 I have plotted the band 9 continuum emission with the contours of the blueshifted and redshifted outflow components from the 0.24" resolution ALMA [CI] map (Cicone et al. (2018b)) overlaid. In figures 4.3 and 4.4 I have plotted the [CI] red and blue wings with contours from band 9 overplotted (i.e. the inverse of figures 4.1 and 4.2). I have also plotted band 8 with contours from the [CI] bluewing overplotted, see figure 4.5. The position of the peak of the red wing and the peak of the blue wing in addition to the two AGNs are marked as red, blue and black crosses respectively.

The first thing to notice is the position of the peak of the [CI] red wing. It is *exactly* at the peak of the continuum emission in band 9, source C-4. This may indicate that the source that heats the dust in this region, is the same source that launches the redshifted outflow (an AGN or a starburst). Alternatively, star formation occurring in the outflow (redshifted side) is powering the source C-4. This close relation between C-4 and the [CI] redwing is also supported by the shape of the red wing contours around C-4 in the band 9 map (figure 4.2), and also the reverse with band 9 contours overlapping the redshifted emission map (figure 4.3). The peak of the blueshifted outflow, on the other hand, is very close to the C-3 peak observed north of AGN-S in band 9 (figure 4.1), with the contours of the bluewing following the emission in band 8 very well (figure 4.5).

The spatial correlation between the dust and the outflows supports the idea of star formation occurring within the outflows (Maiolino et al. (2017)). The large amount of extended continuum emission in NGC6240 (32% of total emission in band 7) suggests that star formation in outflows actually constitutes a significant part of the total submm/mm emission. This is in contrast with previous assumptions that the source of the continuum emission is mainly star formation within the gas in the central region (Engel, H. et al. (2010)) or directly associated with the two AGNs (Treister et al. (2020)). It may rather be an even more intricate explanation, involving large amounts of outflowing, dusty molecular gas. I will further discuss the contribution of extended dust emission to the total flux in section 4.2, and come back to the two point sources C-3 and C-4 in addition to C-11 in section 4.3.

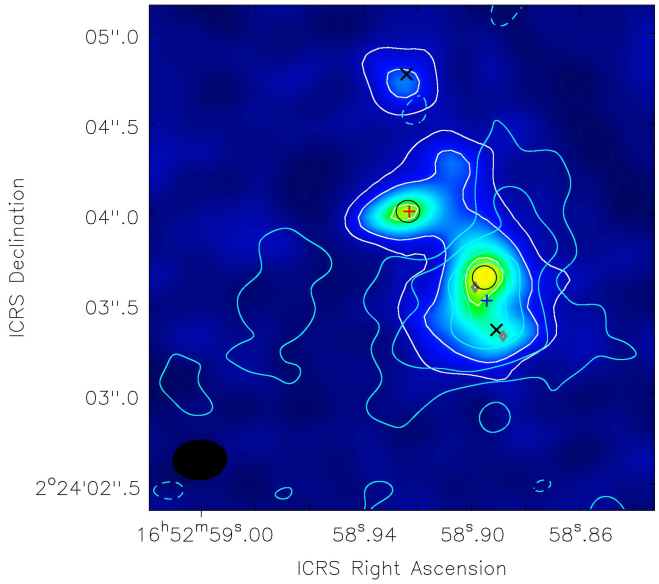

Figure 4.1: Band 9 continuum emission with white contours at [-3, 3, 6, 12, 24, 48] σ. CI(1-0) blueshifted contours (cyan) are overlapped. The two AGNs are marked as black crosses (positions from Hagiwara et al. (2011)), the red and blue wing peaks as red and blue crosses (positions from Cicone et al. (2018b)), and the VLBI radio sources as gray diamonds (Hagiwara et al. (2011)). C-3 and C-4 are marked as black circles, where C-3 is closest to the southern AGN. This figure shows that the [CI] blue wing peak coincides with a peak in band 9 continuum (source C-3) as well as with a radio VLBI source (gray diamond).

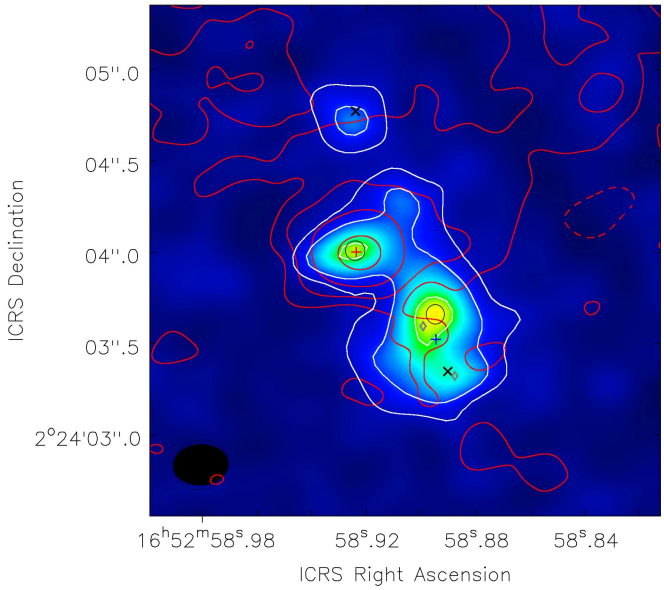

Figure 4.2: Band 9 continuum emission with white contours at [-3, 3, 6, 12, 24, 48] σ. CI(1-0) redshifted contours (red) are overlapped. The two AGNs are marked as black crosses (positions from Hagiwara et al. (2011)), the red and blue wing peaks as red and blue crosses (positions from Cicone et al. (2018b)), and the VLBI radio sources as gray diamonds (Hagiwara et al. (2011)). C-3 and C-4 are marked as black circles, where C-3 is closest to the southern AGN. This figure shows that the [CI] red wing peak coincides with a peak in band 9 continuum source (C-4).

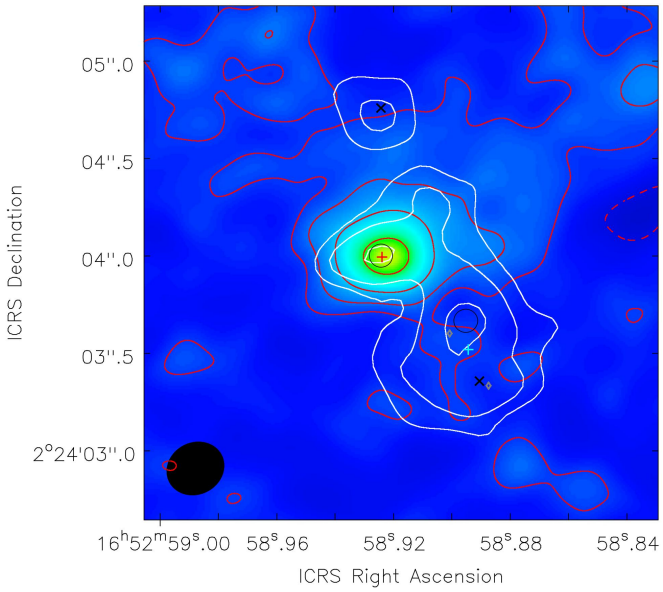

Figure 4.3: CI(1-0) red wing map with band 9 contours (white) overlapping. The AGNs are marked as black crosses (positions from Hagiwara et al. (2011)), the red and blue wing peaks as red and cyan crosses (positions from Cicone et al. (2018b)), and the VLBI radio sources as gray diamonds (Hagiwara et al. (2011)). C-3 and C-4 are marked as black circles, where C-3 is closest to the southern AGN. This map is the inverse of figure 4.2 and shows the coincidence between the [CI] red wing peak and the central peak in the band 9 continuum emission (C-4).

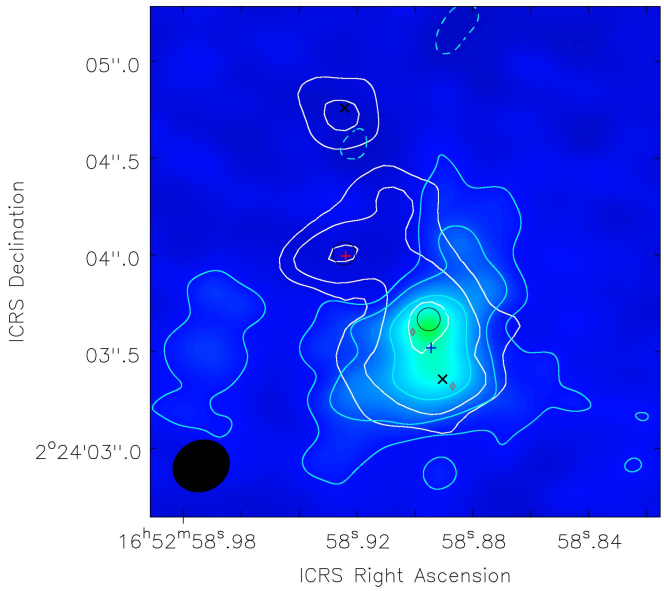

Figure 4.4: CI(1-0) blue wing map with band 9 contours (white) overlapping. The AGNs are marked as black crosses (positions from Hagiwara et al. (2011)), the red and blue wing peaks as red and blue crosses (positions from Cicone et al. (2018b)), and the VLBI radio sources as gray diamonds (Hagiwara et al. (2011)). C-3 and C-4 are marked as black circles, where C-3 is closest to the southern AGN. This map is the inverse of figure 4.1 and shows the coincidence between the [CI] blue wing peak and the source C-3.

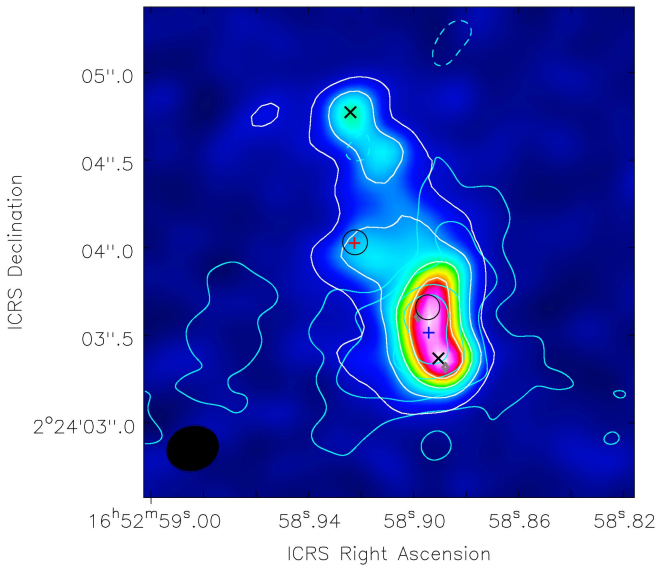

Figure 4.5: Band 8 data with CI(1-0) blue wing contours (cyan) overplotted. The AGNs are marked as black crosses (positions from Hagiwara et al. (2011)), the red and blue wing peaks as red and blue crosses (positions from Cicone et al. (2018b)), and the VLBI radio sources as gray diamonds (Hagiwara et al. (2011)). C-3 and C-4 are marked as black circles, where C-3 is closest to the southern AGN. This map shows the coincidence between the [CI] blue wing peak and the continuum peak in band 8.

4.2 SED in the (Sub)-mm Regime and Extended Emission

In figures 4.6, 4.7, and 4.8, I show the total SED fitted with the MICHI2 model (Liu et al. (2021)) in comparison with my own datapoints. Figure 4.6 shows the total flux, figure 4.7 shows the fluxes in the large and small boxes and figure 4.8 shows the point sources.

My ALMA measurements follow the slope of the modeled SED. The datapoints are however lower than the MICHI2 fit, and also lower than the previous observations at the same wavelengths (figure 4.6). Here I return to the point I made in section 2.1 about the datasets. These are archival data and the observations were *not* designed for measuring the continuum emission or the total flux of this source. The source is very extended, so in fact any interferometric observation would miss some flux, especially single-pointing observations. When looking at the field of view (FoV) of the observations listed in table 2.1, we see that even in our best case at band 3, with a FoV of 63 arcseconds and the largest maximum recoverable scale (MRS) of all the datasets, it is not covering the full continuum source, which is extended by $\sim$ 1 arcminute (see figure 1.3). This is in contrast with the data in the IR/submm bands used in the SED fit, which are mostly satellite data whose FoV covers the entire galaxy (see Liu et al. (2021) and references therein).

Even though my analysis is missing some flux compared to satellite IR data, I am still more sensitive to extended flux than most previous interferometric works who only focused on the central two AGNs. This analysis confirms that there are indeed some extra-nuclear components that likely contribute to the total flux measured by satellites but were missed (or ignored) by previous high resolution interferometric analysis (e.g Scoville et al. (2014)), as we can see that a fraction of the total continuum flux (probed by satellite data) is *not* in the central region or the FoV probed by ALMA. Some of this extended emission is detected in this work, as visualized in the SED plot of the two boxes (figure 4.7) and seen from the continuum maps, but the difference in the total flux tells us that we are still missing additional continuum components. This is to be expected as we are using archival data with limited sensitivity, FoV, and MRS.

An interesting observation to note is the slope of the datapoints from the large box at longer (millimeter) wavelenghts. Here we clearly see that the flux increases from band 4 to band 3. This wavelength region is usually associated with non thermal emission from AGNs (synchrotron emission). The flux increase detected here shows however that this is not always the case. Remember that the large box does not include emission from either of the two AGNs, neither the new point sources detected in this work. It has however been suggested that synchrotron emission is associated with shocks in outflows (Cicone et al. (2018b)). This observation tells us therefore that one should be careful to use this property of the SED as a direct tracer for AGN activity.

The SED of the point sources (figure 4.8) includes the two known AGNs and the three point sources detected in this work. C-11 does not show the same SED rise at low frequencies as the two known AGNs, which is due to non-thermal components. We can therefore rule out the possibility of this being an AGN, which is also confirmed by Chandra X-ray observations where no X-ray counterpart is detected (Valentina Braito,

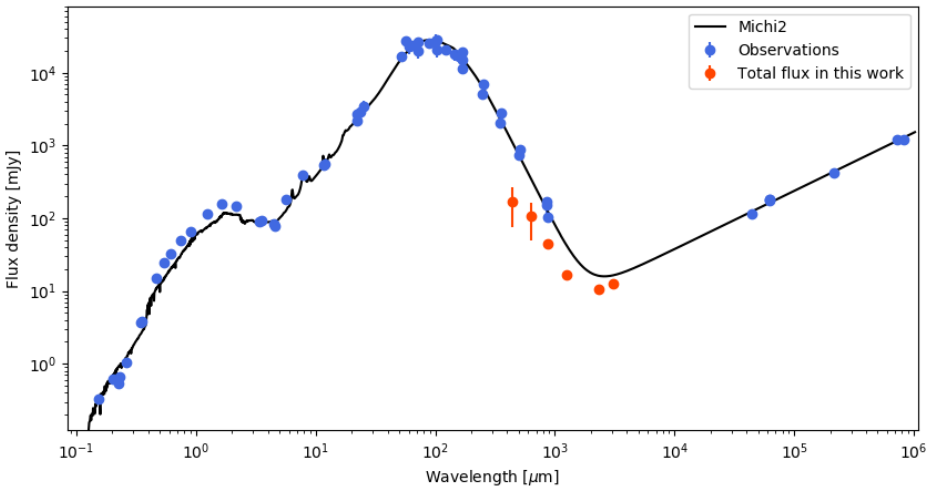

Figure 4.6: The SED of the total flux measured in band 3 to 9 in this work, together with previous observations and the Michi2 fit (Liu et al. (2021)).

private communication). If this was indeed an AGN, we should see X-ray emission originating from the hot corona or the soft X-ray excess.

C-4 and C-3, however, follow the same rising SED at lower frequencies as observed for the two AGNs. They are also clearly associated with the peaks of the molecular outflow. A point source in the radio has also been detected by the Very Large Baseline Interferometer (VLBI) (Hagiwara et al. (2011)) close to C-3 (see figure 4.2), which might be indicative of AGN activity or a very compact radio jet.

4.3 Additional Point Sources

As described above, two of the new point sources detected in this work (C-4 and C-3 in the region between the two AGNs) show characteristics related to AGN activity. If these are indeed two additional AGNs, it would explain the launching base of the outflow (puzzlingly found to be between the two AGNs, see Cicone et al. (2018b), Treister et al. (2020)), and strengthen the theory that this galaxy is dominated by AGN feedback. It would also help explaining the chaotic nature of this galaxy, as two additional galaxies involved in this merger would lead to an enhanced rate of tidal disruptions, increase the redistribution of gas and dust in the ISM, and trigger more star formation and AGN activity, which again would explain why we see so much extended continuum emission.

We cannot, however, rule out the possibility of these being starbursts instead. A massive outflow could drive dust outwards, and the presence of cold and dense gas in the outflow (as suggested by Cicone et al. (2018b)), could make star formation within the outflow possible. As mentioned in section 4.2, one should also be careful using the slope of the SED as a tracer for AGN activity.

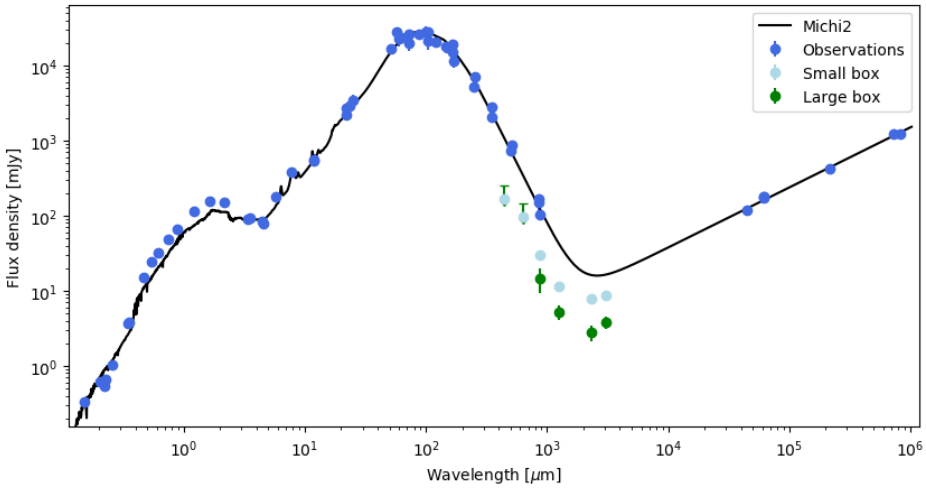

Figure 4.7: The SED of the flux measured in the nuclear region (small box) and an extended region (large box) in band 3 to 9, together with previous observations and the Michi2 fit (Liu et al. (2021)). The datapoints at band 8 and 9 (the two leftmost points) for the large box are upper limits.

The faintness of the mm emission (band 3) is however a good indication of the opposite (no AGN activity) and is what we observe for the north-eastern point source, C-11. In combination with the absence of an X-ray counterpart, we can safely conclude that this is not an AGN. Instead, this source could possibly be the inactive nucleus of another galaxy involved in the merger, or the compact SF nucleus of an obscured tidal dwarf. We know that NGC6240 has prominent tidal features, and the extended continuum emission in this galaxy suggests that there should be several continuum components outside the nuclear region. This means that there is enough cold and dense gas in these regions to trigger star formation, and possibly new stellar systems. This is certainly more likely if the other two point sources are AGNs or nuclei of additional galaxies, as this would create more extreme environments with gas and dust distributed at large distances.

The detection of point sources associated with multiple hidden AGNs in galaxies is interesting from an observational point of view. As dual/binary AGNs are challenging to detect (see section 1.1.3), the potential for these multiwavelength submm/mm continuum analyses to discover obscured AGNs is very promising.

The possible detection of multiple nuclei in a local merger is of great importance from a cosmological point of view as well. Multiple mergers lead to faster growth of galaxies, and could therefore help understanding the hierarchical galaxy formation model. Such galaxies are considered rare in the local universe (Kulkarni and Loeb (2012)), but might actually be of fundamental importance at higher redshifts. NGC6240 is one of the most studied ULIRGs in the local Universe, but still unveils new features.

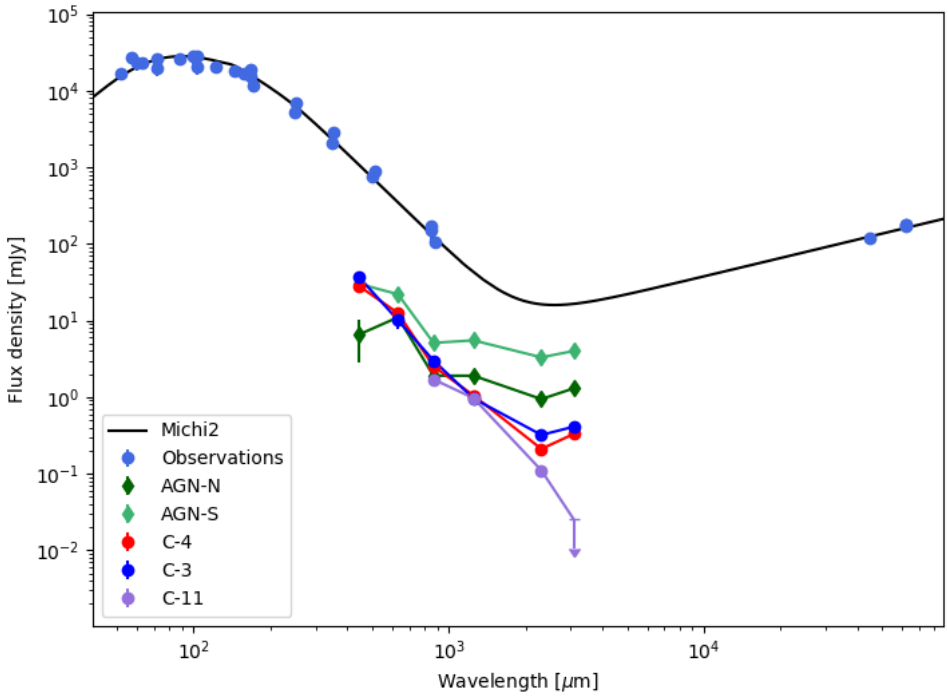

Figure 4.8: The SED of the flux measured at 5 point sources in band 3 to 9, together with previous observations and the Michi2 fit (Liu et al. (2021)).

Chapter 5

Conclusion

In this work I have analyzed the (sub)-mm continuum emission in the local merger NGC6240 to look for extended emission related to processes outside the nuclear region, such as tidal tails and outflows. I did this by exploiting high sensitivity ALMA observations. These archival datasets were not designed for observing the continuum emission, so in order to avoid line contamination, I inspected each spectral window and excluded ranges that contained line emissions. I created high resolution line-free continuum maps in the frequency range from 84 GHz to 680 GHz. I also created low resolution continuum maps that are more sensitive to extended emission. From these maps I measured the fluxes in a nuclear box (1.5 kpc x 1.5 kpc) and an extended box (4.2 kpc x 3.3 kpc, excluding the central 1.5 x 1.5 kpc^2).

This analysis revealed a clearly extended emission beyond the central 1.5 kpc region. From the measurements in the frequency range 336.6-352.2 GHz, the extended emission represents 32 % of the total flux I measure. The shape of the continuum emission is spatially correlated with the redshifted and blueshifted components of the molecular outflow studied in [CI] and CO by previous works (Cicone et al. (2018b)). This can be seen in figures 4.1 and 4.2 where I show a high frequency continuum map with contours from the blueshifted and redshifted emission overplotted. This supports the suggestion that star formation is occurring in these outflows.

I compared my results with a spectral energy distribution (SED) model exploiting previous ground-based and satellite observations (Liu et al. (2021)) of NGC6240. I detected an offset between my ALMA observations of the total flux and the data from the literature. As the archival datasets I used are single-pointing interferometric observations, they have a limited field of view (FoV 63" in band 3, but only 22" in band 9), and are therefore not sensitive to continuum components on larger scales. This suggests that I am still missing some flux compared to satellite data, which means that the fraction of extended emission I calculated is only a lower limit.

From the SED of the extra-nuclear region (with no AGN activity), I detected a flux increase from the datapoints at 130 GHz to 97 GHz. This long wavelength part of the SED is often associated with AGN activity, but it is suggested that this emission may also be attributed to synchrotron emission from outflows. The flux increase I detected

supports this theory.

Three point sources were detected in this work, denoted C-3, C-4 and C-11. C-3 and C-4 are found in between the two known AGNs, and their positions strongly correlate with the peaks of the redshifted and blueshifted components of the molecular outflow as imaged in [CI] (Cicone et al. (2018b)). From the SED plot with data from the two central sources, I found that they follow a similar SED trend as the two known AGNs, with an increase at longer wavelengths associated with AGN activity. C-3 also has a point source counterpart in VLBI readio images, which may indicate synchrotron emission in the radio jets from an AGN. The SED and the radio counterpart of source C-3 indicate this could be an additional obscured AGN. It is possible, however, that these sources are clusters of supernovae (starburst nuclei) instead, which might also be responsible for driving outflows. Additional high resolution observations at multiple wavelengths are needed to constrain this. The third source detected in this work (C-11) does not follow the same slope of the AGNs in the SED, and does not have a counterpart in the X-ray. This suggests that this is probably not an AGN, but possibly another starburst, either associated with a tidal dwarf or with another galaxy participating to the merger. These hypotheses need to be investigated with additional dedicated observations.

NGC6240 is a chaotic galaxy, which this analysis also confirms. In this work I have however proved that there is a significant continuum emission beyond the nuclei, which means that the widespread cold gas detected in previous works both in outflows and in tidal tails has a continuum counterpart outside the nuclear region. The close spatial relation between the extended continuum emission and the outflows also supports this. The detection of the two point sources in the central region might even explain the launching position of the outflows. In any case, it contributes to explain the chaotic nature of the galaxy, especially if these are nuclei of two additional galaxies in this system. A possible third nucleus in the northeast or a tidal tail galaxy might also help explain the intricate morphology of this source.

Future studies targeting spectral ranges without line emission would achieve a higher signal to noise, and further constrain the flux measurements in this work. As there are possibly several continuum components outside the field of view in these observations, I also put forward the need for high resolution observations sensitive to larger fields of the galaxy. This would help estimating the fraction of extended emission contributing to the total emission. As there are very few observations contributing to the long wavelength part of the SED of NGC6240, studies in the far-IR to radio would contribute in constraining the SED further, and give greater insight into the components that dominate at these wavelengths. The launch of James Webb Space Telescope (Gardner et al. (2006)) in October 2021 is especially interesting in this regard.

Bibliography

Ade, P. A. R., Aghanim, N., Arnaud, M., Ashdown, M., Aumont, J., Baccigalupi, C., Banday, A. J., Barreiro, R. B., Bartlett, J. G., and et al. (2016). Planck2015 results. *Astronomy Astrophysics*, 594:A13.

Aguirre, A., Hernquist, L., Schaye, J., Katz, N., Weinberg, D. H., and Gardner, J. (2001). Metal enrichment of the intergalactic medium in cosmological simulations. *The Astrophysical Journal*, 561(2):521–549.

Arribas, S., Colina, L., Bellocchi, E., Maiolino, R., and Villar-Martín, M. (2014). Ionized gas outflows and global kinematics of low-zluminous star-forming galaxies. *Astronomy Astrophysics*, 568:A14.

Baan, W. A., Hagiwara, Y., and Hofner, P. (2007). Hiand oh absorption toward ngc 6240. *The Astrophysical Journal*, 661(1):173â184.

Barkana, R. and Loeb, A. (2001). In the beginning: the first sources of light and the reionization of the universe. *Physics Reports*, 349(2):125â238.

Barnes, J. E. (1988). Encounters of Disk/Halo Galaxies. , 331:699.

Barnes, J. E. and Hernquist, L. (1992). Dynamics of interacting galaxies. , 30:705–742.

Beckmann, V. and Shrader, C. R. (2013). The agn phenomenon: open issues.

Bigiel, F., Leroy, A., Walter, F., Brinks, E., de Blok, W. J. G., Madore, B., and Thornley, M. D. (2008). The star formation law in nearby galaxies on sub-kpc scales. *The Astronomical Journal*, 136(6):2846â2871.

Boesgaard, A. M. and Steigman, G. (1985). Big Bang nucleosynthesis: theories and observations. , 23:319–378.

Boquien, M., Burgarella, D., Roehlly, Y., Buat, V., Ciesla, L., Corre, D., Inoue, A. K., and Salas, H. (2019). Cigale: a python code investigating galaxy emission. *Astronomy Astrophysics*, 622:A103.

Bot, C., Ysard, N., Paradis, D., Bernard, J. P., Lagache, G., Israel, F. P., and Wall, W. F. (2010). Submillimeter to centimeter excess emission from the magellanic clouds. *Astronomy Astrophysics*, 523:A20.

Bournaud, F., Chapon, D., Teyssier, R., Powell, L. C., Elmegreen, B. G., Elmegreen, D. M., Duc, P.-A., Contini, T., Epinat, B., and Shapiro, K. L. (2011). Hydrodynamics of high-redshift galaxy collisions: From gas-rich disks to dispersion-dominated mergers and compact spheroids. *The Astrophysical Journal*, 730(1):4.

Bouwens, R. J., Illingworth, G. D., Oesch, P. A., Trenti, M., Labbé, I., Bradley, L., Carollo, M., van Dokkum, P. G., Gonzalez, V., Holwerda, B., and et al. (2015). Uv luminosity functions at redshiftszâ$\frac{1}{4}$ 4 tozâ$\frac{1}{4}$ 10: 10,000 galaxies fromhstlegacy fields. *The Astrophysical Journal*, 803(1):34.

Bower, R. G., Benson, A. J., and Crain, R. A. (2012). What shapes the galaxy mass function? Exploring the roles of supernova-driven winds and active galactic nuclei. *Monthly Notices of the Royal Astronomical Society*, 422(4):2816–2840.

Brinchmann, J., Charlot, S., White, S. D. M., Tremonti, C., Kauffmann, G., Heckman, T., and Brinkmann, J. (2004). The physical properties of star-forming galaxies in the low-redshift Universe. , 351(4):1151–1179.

Capelo, P. R., Dotti, M., Volonteri, M., Mayer, L., Bellovary, J. M., and Shen, S. (2017). A survey of dual active galactic nuclei in simulations of galaxy mergers: frequency and properties. *Monthly Notices of the Royal Astronomical Society*, 469(4):4437â4454.

Cattaneo, A. (2001). Quasars and galaxy formation. *Monthly Notices of the Royal Astronomical Society*, 324(1):128–140.

Cazzoli, S. (2017). Negative and positive outflow-feedback in nearby (u)lirgs. *Frontiers in Astronomy and Space Sciences*, 4:62.

Chu, J. K., Sanders, D. B., Larson, K. L., Mazzarella, J. M., Howell, J. H., Díaz-Santos, T., Xu, K. C., Paladini, R., Schulz, B., Shupe, D., Appleton, P., Armus, L., Billot, N., Chan, B. H. P., Evans, A. S., Fadda, D., Frayer, D. T., Haan, S., Ishida, C. M., Iwasawa, K., Kim, D. C., Lord, S., Murphy, E., Petric, A., Privon, G. C., Surace, J. A., and Treister, E. (2017). The Great Observatories All-Sky LIRG Survey: Herschel Image Atlas and Aperture Photometry. , 229(2):25.

Cicone, C., Brusa, M., Ramos Almeida, C., Cresci, G., Husemann, B., and Mainieri, V. (2018a). The largely unconstrained multiphase nature of outflows in agn host galaxies. *Nature Astronomy*, 2(3):176â178.

Cicone, C., Severgnini, P., Papadopoulos, P. P., Maiolino, R., Feruglio, C., Treister, E., Privon, G. C., Zhang, Z.-y., Ceca, R. D., Fiore, F., and et al. (2018b). Alma [c i]3 p 1â3 p 0 observations of ngc 6240: A puzzling molecular outflow, and the role of outflows in the global Î±$cofactorof(u)lirgs.TheAstrophysicalJournal$, 863(2) : 143.

Clements, D. L., Pearson, C., Farrah, D., Greenslade, J., Bernard-Salas, J., González-Alfonso, E., Afonso, J., Efstathiou, A., Rigopoulou, D., Lebouteiller, V., Hurley, P. D., and Spoon, H. (2018). HERUS: the far-IR/submm spectral energy distributions of local ULIRGs and photometric atlas. , 475(2):2097–2121.

Colbert, E. J. M., Wilson, A. S., and Bland-Hawthorn, J. (1994). The Radio Emission from the Ultraluminous Far-Infrared Galaxy NGC 6240. , 436:89.

Colless, M., Dalton, G., Maddox, S., Sutherland, W., Norberg, P., Cole, S., Bland-Hawthorn, J., Bridges, T., Cannon, R., Collins, C., Couch, W., Cross, N., Deeley, K., De Propris, R., Driver, S. P., Efstathiou, G., Ellis, R. S., Frenk, C. S., Glazebrook, K., Jackson, C., Lahav, O., Lewis, I., Lumsden, S., Madgwick, D., Peacock, J. A., Peterson, B. A., Price, I., Seaborne, M., and Taylor, K. (2001). The 2dF Galaxy Redshift Survey: spectra and redshifts. , 328(4):1039–1063.

Conselice, C. J. (2007). Galaxy Mergers and Interactions at High Redshift. In Combes, F. and Palouš, J., editors, *Galaxy Evolution across the Hubble Time*, volume 235, pages 381–384.

Costa, T., Sijacki, D., and Haehnelt, M. G. (2014). Feedback from active galactic nuclei: energy- versus momentum-driving. *Monthly Notices of the Royal Astronomical Society*, 444(3):2355â2376.

Costa, T., Sijacki, D., and Haehnelt, M. G. (2015). Fast cold gas in hot AGN outflows. *Monthly Notices of the Royal Astronomical Society: Letters*, 448(1):L30–L34.

Croton, D. J., Springel, V., White, S. D. M., De Lucia, G., Frenk, C. S., Gao, L., Jenkins, A., Kauffmann, G., Navarro, J. F., and Yoshida, N. (2006). The many lives of active galactic nuclei: cooling flows, black holes and the luminosities and colours of galaxies. , 365(1):11–28.

Cunha, E. d., Walter, F., Smail, I. R., Swinbank, A. M., Simpson, J. M., Decarli, R., Hodge, J. A., Weiss, A., Werf, P. P. v. d., Bertoldi, F., and et al. (2015). An alma survey of sub-millimeter galaxies in the extendedchandradeep field south: Physical properties derived from ultraviolet-to-radio modeling. *The Astrophysical Journal*, 806(1):110.

Daddi, E., Bournaud, F., Walter, F., Dannerbauer, H., Carilli, C. L., Dickinson, M., Elbaz, D., Morrison, G. E., Riechers, D., Onodera, M., Salmi, F., Krips, M., and Stern, D. (2010). Very High Gas Fractions and Extended Gas Reservoirs in z = 1.5 Disk Galaxies. , 713(1):686–707.

Davé, R., Oppenheimer, B. D., and Finlator, K. (2011). Galaxy evolution in cosmological simulations with outflows - I. Stellar masses and star formation rates. , 415(1):11–31.

Davé, R., Oppenheimer, B. D., and Finlator, K. (2011). Galaxy evolution in cosmological simulations with outflows â I. Stellar masses and star formation rates. *Monthly Notices of the Royal Astronomical Society*, 415(1):11–31.

de Bernardis, P., Ade, P. A. R., Bock, J. J., Bond, J. R., Borrill, J., Boscaleri, A., Coble, K., Crill, B. P., De Gasperis, G., Farese, P. C., and et al. (2000). A flat universe from high-resolution maps of the cosmic microwave background radiation. *Nature*, 404(6781):955â959.

Di Matteo, T., Springel, V., and Hernquist, L. (2005). Energy input from quasars regulates the growth and activity of black holes and their host galaxies. *Nature*, 433(7026):604â607.

Dole, H., Lagache, G., Puget, J.-L., Gispert, R., Aussel, H., Bouchet, F., Ciliegi, C., Clements, D., Cesarsky, C., Désert, F.-X., Elbaz, D., Franceschini, A., Guiderdoni, B., Harwit, M., Laureijs, R., Lemke, D., McMahon, R., Moorwood, A., Oliver, S., and Stickel, M. (1999). Firback survey with iso: data reduction, analysis and first results. 427:1031.

Draine, B. T. (1978). Photoelectric heating of interstellar gas. , 36:595–619.

Draine, B. T. and Li, A. (2007). Infrared Emission from Interstellar Dust. IV. The Silicate-Graphite-PAH Model in the Post-Spitzer Era. , 657(2):810–837.

Drake, A. B., Garel, T., Wisotzki, L., Leclercq, F., Hashimoto, T., Richard, J., Bacon, R., Blaizot, J., Caruana, J., Conseil, S., and et al. (2017). The muse hubble ultra deep field survey. *Astronomy Astrophysics*, 608:A6.

Eales, S., Dunne, L., Clements, D., Cooray, A., De Zotti, G., Dye, S., Ivison, R., Jarvis, M., Lagache, G., Maddox, S., and et al. (2010). The herschel atlas. *Publications of the Astronomical Society of the Pacific*, 122(891):499â515.

Engel, H., Davies, R. I., Genzel, R., Tacconi, L. J., Hicks, E. K. S., Sturm, E., Naab, T., Johansson, P. H., Karl, S. J., Max, C. E., Medling, A., and van der Werf, P. P. (2010). Ngc0: merger-induced star formation and gas dynamics. *A&A*, 524:A56.

Fabian, A. (2012). Observational evidence of active galactic nuclei feedback. *Annual Review of Astronomy and Astrophysics*, 50(1):455â489.

Fabian, A. C. (1999). Active galactic nuclei. *Proceedings of the National Academy of Sciences*, 96(9):4749–4751.

Faucher-Giguére, C.-A. and Quataert, E. (2012). The physics of galactic winds driven by active galactic nuclei. *Monthly Notices of the Royal Astronomical Society*, 425(1):605â622.

Ferrarese, L. and Ford, H. (2005). Supermassive black holes in galactic nuclei: Past, present and future research. *Space Science Reviews*, 116(3-4):523â624.

Feruglio, C., Fiore, F., Maiolino, R., Piconcelli, E., Aussel, H., Elbaz, D., Le Floc'h, E., Sturm, E., Davies, R., and Cicone, C. (2013a). <ASTROBJ>NGC 6240</ASTROBJ>: extended CO structures and their association with shocked gas. , 549:A51.

Feruglio, C., Fiore, F., Piconcelli, E., Cicone, C., Maiolino, R., Davies, R., and Sturm, E. (2013b). High resolution mapping of CO(1-0) in NGC 6240. , 558:A87.

Galliano, F., Galametz, M., and Jones, A. P. (2018). The interstellar dust properties of nearby galaxies. *Annual Review of Astronomy and Astrophysics*, 56(1):673â713.

Gardner, J. P., Mather, J. C., Clampin, M., Doyon, R., Greenhouse, M. A., Hammel, H. B., Hutchings, J. B., Jakobsen, P., Lilly, S. J., Long, K. S., and et al. (2006). The james webb space telescope. *Space Science Reviews*, 123(4):485â606.

Gerssen, J., van der Marel, R. P., Axon, D., Mihos, J. C., Hernquist, L., and Barnes, J. E. (2004). Hubble Space Telescope Observations of NGC 6240: A Case Study of an Ultraluminous Infrared Galaxy with Obscured Activity. , 127(1):75–89.

Ghisellini, G. (2013). Radiative processes in high energy astrophysics. *Lecture Notes in Physics*.

Giavalisco, M., Dickinson, M., Ferguson, H. C., Ravindranath, S., Kretchmer, C., Moustakas, L. A., Madau, P., Fall, S. M., Gardner, J. P., Livio, M., and et al. (2004). The rest-frame ultraviolet luminosity density of star-forming galaxies at redshifts z $>$ 3.5. *The Astrophysical Journal*, 600(2):L103âL106.

Gott, J. R., I. and Rees, M. J. (1975). A theory of galaxy formation and clustering. , 45:365–376.

Gould, R. J. and Salpeter, E. E. (1963). The Interstellar Abundance of the Hydrogen Molecule. I. Basic Processes. , 138:393.

Guth, A. H. (1981). Inflationary universe: A possible solution to the horizon and flatness problems. *Phys. Rev. D*, 23:347–356.

Hagiwara, Y., Baan, W. A., and Klöckner, H.-R. (2011). Very long baseline interferometry observations of ngc 6240: Resolving the double nuclei and radio supernovae. *The Astronomical Journal*, 142(1):17.

Harrison, C. M. (2014). Observational constraints on the influence of active galactic nuclei on the evolution of galaxies.

Hernquist, L. (1992). Structure of Merger Remnants. I. Bulgeless Progenitors. , 400:460.

Hibbard, J. E. and van Gorkom, J. H. (1996). HI, HII, and R-Band Observations of a Galactic Merger Sequence. , 111:655.

Hibbard, J. E. and Yun, M. S. (1999). A 180 kiloparsec tidal tail in the luminous infrared merger arp 299. *The Astronomical Journal*, 118(1):162â185.

Hickox, R. C. and Alexander, D. M. (2018). Obscured active galactic nuclei. *Annual Review of Astronomy and Astrophysics*, 56(1):625â671.

Högbom, J. (2003). Early work in imaging. 300:17.

Högbom, J. A. (1974). Aperture Synthesis with a Non-Regular Distribution of Interferometer Baselines. , 15:417.

Hopkins, A. M. (2004). On the evolution of starâforming galaxies. *The Astrophysical Journal*, 615(1):209â221.

Hopkins, P. F., Hernquist, L., Cox, T. J., and Keres, D. (2008). A cosmological framework for the coâevolution of quasars, supermassive black holes, and elliptical galaxies. i. galaxy mergers and quasar activity. *The Astrophysical Journal Supplement Series*, 175(2):356â389.

Hopkins, P. F., Keres, D., Oñorbe, J., Faucher-GiguÃ¨re, C.-A., Quataert, E., Murray, N., and Bullock, J. S. (2014). Galaxies on fire (feedback in realistic environments): stellar feedback explains cosmologically inefficient star formation. *Monthly Notices of the Royal Astronomical Society*, 445(1):581â603.

Hopkins, P. F., Quataert, E., and Murray, N. (2012). Stellar feedback in galaxies and the origin of galaxy-scale winds. *Monthly Notices of the Royal Astronomical Society*, 421(4):3522â3537.

Hubble, E. (1929). A relation between distance and radial velocity among extra-galactic nebulae. *Proceedings of the National Academy of Sciences*, 15(3):168–173.

Hung, C.-L., Sanders, D. B., Casey, C. M., Lee, N., Barnes, J. E., Capak, P., Kartaltepe, J. S., Koss, M., Larson, K. L., Le Flocâh, E., and et al. (2013). The role of galaxy interaction in the sfr-m*relation: Characterizing morphological properties ofherschel-selected galaxies at 0.2 <z< 1.5. *The Astrophysical Journal*, 778(2):129.

Ilbert, O., Arnouts, S., McCracken, H. J., Bolzonella, M., Bertin, E., Le FÃ¨vre, O., Mellier, Y., Zamorani, G., PellÃ^2, $R., Iovino, A., and et al.$(2006).$Accurate photometric redshifts for the cfht legacy survey calibrated$ 841856.

Iono, D., Wilson, C. D., Takakuwa, S., Yun, M. S., Petitpas, G. R., Peck, A. B., Ho, P. T. P., Matsushita, S., Pihlstrom, Y. M., and Wang, Z. (2007). High-Resolution Imaging of Warm and Dense Molecular Gas in the Nuclear Region of the Luminous Infrared Galaxy NGC 6240. , 659(1):283–295.

Kellermann, K. I., Lister, M. L., Homan, D. C., Vermeulen, R. C., Cohen, M. H., Ros, E., Kadler, M., Zensus, J. A., and Kovalev, Y. Y. (2004). Sub-Milliarcsecond Imaging of Quasars and Active Galactic Nuclei. III. Kinematics of Parsec-scale Radio Jets. , 609(2):539–563.

Kennicutt, Robert C., J. (1998). The Global Schmidt Law in Star-forming Galaxies. , 498(2):541–552.

Kilerci Eser, E., Goto, T., and Doi, Y. (2014). Ultraluminous infrared galaxies in theakariall-sky survey. *The Astrophysical Journal*, 797(1):54.

Klein, U., Lisenfeld, U., and Verley, S. (2018). Radio synchrotron spectra of star-forming galaxies. *A&A*, 611:A55.

Kleinmann, D. E. and Low, F. J. (1970). Observations of Infrared Galaxies. , 159:L165.

Kulkarni, G. and Loeb, A. (2012). Formation of galactic nuclei with multiple supermassive black holes at high redshifts. *Monthly Notices of the Royal Astronomical Society*, 422(2):1306â1323.

Laor, A. and Behar, E. (2008). On the origin of radio emission in radio-quiet quasars. *Monthly Notices of the Royal Astronomical Society*, 390(2):847â862.

Leroy, A. K., Walter, F., Brinks, E., Bigiel, F., de Blok, W. J. G., Madore, B., and Thornley, M. D. (2008). The Star Formation Efficiency in Nearby Galaxies: Measuring Where Gas Forms Stars Effectively. , 136(6):2782–2845.

Lisenfeld, U., Isaak, K. G., and Hills, R. (2000). Dust and gas in luminous infrared galaxies - results from SCUBA observations. , 312(2):433–441.

Liu, D., Daddi, E., Schinnerer, E., Saito, T., Leroy, A., Silverman, J. D., Valentino, F., Magdis, G. E., Gao, Y., Jin, S., and et al. (2021). Co excitation, molecular gas density, and interstellar radiation field in local and high-redshift galaxies. *The Astrophysical Journal*, 909(1):56.

Lonsdale, C., del Carmen Polletta, M., Surace, J., Shupe, D., Fang, F., Xu, C. K., Smith, H. E., Siana, B., Rowan-Robinson, M., Babbedge, T., Oliver, S., Pozzi, F., Davoodi, P., Owen, F., Padgett, D., Frayer, D., Jarrett, T., Masci, F., O'Linger, J., Conrow, T., Farrah, D., Morrison, G., Gautier, N., Franceschini, A., Berta, S., Perez-Fournon, I., Hatziminaoglou, E., Afonso-Luis, A., Dole, H., Stacey, G., Serjeant, S., Pierre, M., Griffin, M., and Puetter, R. (2004). First insights into the spitzer wide-area infrared extragalactic legacy survey (SWIRE) galaxy populations. *The Astrophysical Journal Supplement Series*, 154(1):54–59.

Low, J. and Kleinmann, D. E. (1968). Proceedings of the Conference on Seyfert Galaxies and Related Objects: 17. Infrared Observations of Seyfert Galaxies, Quasistellar Sources, and Planetary Nebulae. , 73:868.

Madau, P., Ferguson, H. C., Dickinson, M. E., Giavalisco, M., Steidel, C. C., and Fruchter, A. (1996). High-redshift galaxies in the Hubble Deep Field: colour selection and star formation history to z~4. , 283(4):1388–1404.

Maiolino, R., Russell, H. R., Fabian, A. C., Carniani, S., Gallagher, R., Cazzoli, S., Arribas, S., Belfiore, F., Bellocchi, E., Colina, L., and et al. (2017). Star formation inside a galactic outflow. *Nature*, 544(7649):202â206.

Martínez-Delgado, D., Gabany, R. J., Crawford, K., Zibetti, S., Majewski, S. R., Rix, H.-W., Fliri, J., Carballo-Bello, J. A., Bardalez-Gagliuffi, D. C., Peñarrubia, J., and et al. (2010). Stellar tidal streams in spiral galaxies of the local volume: A pilot survey with modest aperture telescopes. *The Astronomical Journal*, 140(4):962â967.

Max, C. E., Canalizo, G., Macintosh, B. A., Raschke, L., Whysong, D., Antonucci, R., and Schneider, G. (2005). The core of ngc 6240 from keck adaptive optics andhubble space telescopenicmos observations. *The Astrophysical Journal*, 621(2):738â749.

McGurk, R. C., Max, C. E., Medling, A. M., Shields, G. A., and Comerford, J. M. (2015). Spatially Resolved Imaging and Spectroscopy of Candidate Dual Active Galactic Nuclei. , 811(1):14.

McMullin, J., Waters, B., Schiebel, D., Young, W., and Golap, K. (2007). Casa architecture and applications. 376.

Menci, N., Fiore, F., Puccetti, S., and Cavaliere, A. (2008). The blast wave model for agn feedback: Effects on agn obscuration. *The Astrophysical Journal*, 686(1):219â229.

Mo, H., van den Bosch, F. C., and White, S. (2010). *Galaxy Formation and Evolution*.

Morganti, R., Veilleux, S., Oosterloo, T., Teng, S. H., and Rupke, D. (2016). Another piece of the puzzle: The fast hâi outflow in mrk 231. *Astronomy Astrophysics*, 593:A30.

Murakami, H., Baba, H., Barthel, P., Clements, D. L., Cohen, M., Doi, Y., Enya, K., Figueredo, E., Fujishiro, N., Fujiwara, H., Fujiwara, M., Garcia-Lario, P., Goto, T., Hasegawa, S., Hibi, Y., Hirao, T., Hiromoto, N., Hong, S. S., Imai, K., Ishigaki, M., Ishiguro, M., Ishihara, D., Ita, Y., Jeong, W.-S., Jeong, K. S., Kaneda, H., Kataza, H., Kawada, M., Kawai, T., Kawamura, A., Kessler, M. F., Kester, D., Kii, T., Kim, D. C., Kim, W., Kobayashi, H., Koo, B. C., Kwon, S. M., Lee, H. M., Lorente, R., Makiuti, S., Matsuhara, H., Matsumoto, T., Matsuo, H., Matsuura, S., MÃller, T. G., Murakami, N., Nagata, H., Nakagawa, T., Naoi, T., Narita, M., Noda, M., Oh, S. H., Ohnishi, A., Ohyama, Y., Okada, Y., Okuda, H., Oliver, S., Onaka, T., Ootsubo, T., Oyabu, S., Pak, S., Park, Y.-S., Pearson, C. P., Rowan-Robinson, M., Saito, T., Sakon, I., Salama, A., Sato, S., Savage, R. S., Serjeant, S., Shibai, H., Shirahata, M., Sohn, J., Suzuki, T., Takagi, T., Takahashi, H., Tanabé, T., Takeuchi, T. T., Takita, S., Thomson, M., Uemizu, K., Ueno, M., Usui, F., Verdugo, E., Wada, T., Wang, L., Watabe, T., Watarai, H., White, G. J., Yamamura, I., Yamauchi, C., and Yasuda, A. (2007). The Infrared Astronomical Mission AKARI*. *Publications of the Astronomical Society of Japan*, 59(sp2):S369–S376.

Murray, N., Quataert, E., and Thompson, T. A. (2005). On the maximum luminosity of galaxies and their central black holes: Feedback from momentumâdriven winds. *The Astrophysical Journal*, 618(2):569â585.

Nardini, E., Wang, J., Fabbiano, G., Elvis, M., Pellegrini, S., Risaliti, G., Karovska, M., and Zezas, A. (2013). The exceptional soft x-ray halo of the galaxy merger ngc 6240. *The Astrophysical Journal*, 765(2):141.

Netzer, H. (2015). Revisiting the unified model of active galactic nuclei. *Annual Review of Astronomy and Astrophysics*, 53(1):365â408.

Nims, J., Quataert, E., and Faucher-GiguÃ¨re, C.-A. (2015). Observational signatures of galactic winds powered by active galactic nuclei. *Monthly Notices of the Royal Astronomical Society*, 447(4):3612–3622.

Peacock, J. A. (1999). *Cosmological Physics*.

Peng, Y.-j., Lilly, S. J., KovaÄ, K., Bolzonella, M., Pozzetti, L., Renzini, A., Zamorani, G., Ilbert, O., Knobel, C., Iovino, A., and et al. (2010). Mass and environment as drivers of galaxy evolution in sdss and zcosmos and the origin of the schechter function. *The Astrophysical Journal*, 721(1):193â221.

Pereira-Santaella, M., Alonso-Herrero, A., Colina, L., Miralles-Caballero, D., Pérez-González, P. G., Arribas, S., Bellocchi, E., Cazzoli, S., Díaz-Santos, T., and LÃ^3*pez, J. P.*(2015). $Star - formationhistoriesoflocalluminousinfraredgalaxies. AstronomyAstrophysics$, 577 : A78.

Perlmutter, S., Aldering, G., Goldhaber, G., Knop, R. A., Nugent, P., Castro, P. G., Deustua, S., Fabbro, S., Goobar, A., Groom, D. E., Hook, I. M., Kim, A. G., Kim, M. Y., Lee, J. C., Nunes, N. J., Pain, R., Pennypacker, C. R., Quimby, R., Lidman, C., Ellis, R. S., Irwin, M., McMahon, R. G., Ruiz-Lapuente, P., Walton, N., Schaefer, B., Boyle, B. J., Filippenko, A. V., Matheson, T., Fruchter, A. S., Panagia, N., Newberg, H. J. M., Couch, W. J., and Project, T. S. C. (1999). Measurements of Ω and Λ from 42 High-Redshift Supernovae. , 517(2):565–586.

Ren, J., Zheng, X. Z., Valls-Gabaud, D., Duc, P.-A., Bell, E. F., Pan, Z., Qin, J., Shi, D. D., Qiao, M., He, Y., and et al. (2020). Long tidal tails in merging galaxies and their implications. *Monthly Notices of the Royal Astronomical Society*, 499(3):3399â3409.

Ricci, C., Ueda, Y., Paltani, S., Ichikawa, K., Gandhi, P., and Awaki, H. (2014). Iron kÎ±$emissionintype - iandtype - iiactivegalacticnuclei. MonthlyNoticesoftheRoyalAstronomicalSociety$, 441(4) : 36223633.

Rodighiero, G., Daddi, E., Baronchelli, I., Cimatti, A., Renzini, A., Aussel, H., Popesso, P., Lutz, D., Andreani, P., Berta, S., and et al. (2011). The lesser role of starbursts in star formation at z = 2. *The Astrophysical Journal*, 739(2):L40.

Rowan-Robinson, M., Oliver, S., Efstathiou, A., Gruppioni, C., Serjeant, S., Cesarsky, C., Danese, L., Franceschini, A., Genzel, R., Lawrence, A., Lemke, D., McMahon, R., Miley, G., Perez-Fournon, I., Puget, J.-L., Rocca-Volmerange, B., Cileigi, P., Héraudeau, P., Surace, C., and Lafranca, F. (1999). The european large area iso survey: Elais.

Sanders, D. B., Mazzarella, J. M., Kim, D.-C., Surace, J. A., and Soifer, B. T. (2003). Theirasrevised bright galaxy sample. *The Astronomical Journal*, 126(4):1607â1664.

Sanders, D. B. and Mirabel, I. F. (1996). Luminous Infrared Galaxies. , 34:749.

Sanders, D. B., Soifer, B. T., Elias, J. H., Madore, B. F., Matthews, K., Neugebauer, G., and Scoville, N. Z. (1988). Ultraluminous Infrared Galaxies and the Origin of Quasars. , 325:74.

Schmidt, M. (1959). The Rate of Star Formation. , 129:243.

Schneider, E. E., Robertson, B. E., and Thompson, T. A. (2018). Production of cool gas in thermally-driven outflows.

Scoville, N., Sheth, K., Walter, F., Manohar, S., Zschaechner, L., Yun, M., Koda, J., Sanders, D., Murchikova, E., Thompson, T., Robertson, B., Genzel, R., Hernquist, L., Tacconi, L., Brown, R., Narayanan, D., Hayward, C., Barnes, J., Kartaltepe, J., and Fomalont, E. (2014). Alma imaging of hcn, cs, and dust in arp 220 and ngc 6240. *The Astrophysical Journal*, 800.

Severgnini, P., Braito, V., Cicone, C., Saracco, P., Vignali, C., Serafinelli, R., Della Ceca, R., Dotti, M., Cusano, F., Paris, D., Pruto, G., Zaino, A., Ballo, L., and Landoni, M. (2021). A possible sub-kiloparsec dual AGN buried behind the galaxy curtain. , 646:A153.

Smail, I., Ivison, R. J., and Blain, A. W. (1997). A deep submillimeter survey of lensing clusters: A new window on galaxy formation and evolution. *The Astrophysical Journal*, 490(1):L5âL8.

Smith, H. E., Lonsdale, C. J., and Lonsdale, C. J. (1998). The starburst-AGN connection. II. the nature of luminous infrared galaxies as revealed by VLBI, VLA, infrared, and optical observations. *The Astrophysical Journal*, 492(1):137–172.

Soifer, B. T., Rowan-Robinson, M., Houck, J. R., de Jong, T., Neugebauer, G., Aumann, H. H., Beichman, C. A., Boggess, N., Clegg, P. E., Emerson, J. P., Gillett, F. C., Habing, H. J., Hauser, M. G., Low, F. J., Miley, G., and Young, E. (1984). Infrared galaxies in the IRAS minisurvey. , 278:L71–L74.

Somerville, R. S. and Davé, R. (2015). Physical Models of Galaxy Formation in a Cosmological Framework. , 53:51–113.

Springel, V., White, S. D. M., Jenkins, A., Frenk, C. S., Yoshida, N., Gao, L., Navarro, J., Thacker, R., Croton, D., Helly, J., Peacock, J. A., Cole, S., Thomas, P., Couchman, H., Evrard, A., Colberg, J., and Pearce, F. (2005). Simulations of the formation, evolution and clustering of galaxies and quasars. , 435(7042):629–636.

Stawarz, Å., Tanaka, Y. T., Madejski, G., OâSullivan, S. P., Cheung, C. C., Feain, I. J., Fukazawa, Y., Gandhi, P., Hardcastle, M. J., Kataoka, J., and et al. (2013). Giant lobes of centaurus a radio galaxy observed with thesuzakux-ray satellite. *The Astrophysical Journal*, 766(1):48.

Steidel, C. C., Shapley, A. E., Pettini, M., Adelberger, K. L., Erb, D. K., Reddy, N. A., and Hunt, M. P. (2004). A survey of starâforming galaxies in the $1.4 < z < 2.5$ redshift desert: Overview. *The Astrophysical Journal*, 604(2):534â550.

Tacconi, L. J., Genzel, R., Tecza, M., Gallimore, J. F., Downes, D., and Scoville, N. Z. (1999). Gasdynamics in the luminous merger ngc 6240. *The Astrophysical Journal*, 524(2):732â745.

Tecza, M., Genzel, R., Tacconi, L., Anders, S., Tacconi-Garman, L., and Thatte, N. (2008). Stellar dynamics and the implications on the merger evolution in ngc 6240. *The Astrophysical Journal*, 537:178.

Treister, E., Messias, H., Privon, G. C., Nagar, N., Medling, A. M., U, V., Bauer, F. E., Cicone, C., Muñoz, L. B., Evans, A. S., and et al. (2020). The molecular gas in the ngc 6240 merging galaxy system at the highest spatial resolution. *The Astrophysical Journal*, 890(2):149.

Urry, C. M. and Padovani, P. (1995). Unified Schemes for Radio-Loud Active Galactic Nuclei. , 107:803.

Veilleux, S., Cecil, G., and Bland-Hawthorn, J. (2005). Galactic winds. *Annual Review of Astronomy and Astrophysics*, 43(1):769–826.

Veilleux, S., Meléndez, M., Sturm, E., Gracia-Carpio, J., Fischer, J., González-Alfonso, E., Contursi, A., Lutz, D., Poglitsch, A., Davies, R., Genzel, R., Tacconi, L., de Jong, J. A., Sternberg, A., Netzer, H., Hailey-Dunsheath, S., Verma, A., Rupke, D. S. N., Maiolino, R., Teng, S. H., and Polisensky, E. (2013). Fast Molecular Outflows in Luminous Galaxy Mergers: Evidence for Quasar Feedback from Herschel. , 776(1):27.

Wang, J., Nardini, E., Fabbiano, G., Karovska, M., Elvis, M., Pellegrini, S., Max, C., Risaliti, G., U, V., and Zezas, A. (2014). Fast and furious: Shock heated gas as the origin of spatially resolved hard x-ray emission in the central 5 kpc of the galaxy merger ngc 6240. *The Astrophysical Journal*, 781(1):55.

Whitaker, K. E., Franx, M., Leja, J., van Dokkum, P. G., Henry, A., Skelton, R. E., Fumagalli, M., Momcheva, I. G., Brammer, G. B., Labbé, I., and et al. (2014). Constraining the low-mass slope of the star formation sequence at 0.5 <z< 2.5. *The Astrophysical Journal*, 795(2):104.

White, S. D. M. and Rees, M. J. (1978). Core condensation in heavy halos: a two-stage theory for galaxy formation and clustering. , 183:341–358.

Witten, E. (1981). Dynamical breaking of supersymmetry. *Nuclear Physics B*, 188(3):513–554.

Wright, E. L., Eisenhardt, P. R. M., Mainzer, A. K., Ressler, M. E., Cutri, R. M., Jarrett, T., Kirkpatrick, J. D., Padgett, D., McMillan, R. S., Skrutskie, M., and et al. (2010). The wide-field infrared survey explorer (wise): Mission description and initial on-orbit performance. *The Astronomical Journal*, 140(6):1868â1881.

Wright, G. S., Joseph, R. D., and Meikle, W. P. S. (1984). The ultraluminous interacting galaxy NGC6240. , 309(5967):430–431.

Yoshida, M., Yagi, M., Ohyama, Y., Komiyama, Y., Kashikawa, N., Tanaka, H., and Okamura, S. (2016). Giant hÎ±*nebulasurroundingthestarburstmergerngc*6240.*TheAstrophysicalJournal*, 820(1) : 48.

Yuan, T. T., Kewley, L. J., and Sanders, D. B. (2010). The Role of Starburst-Active Galactic Nucleus Composites in Luminous Infrared Galaxy Mergers: Insights from the New Optical Classification Scheme. , 709(2):884–911.

Zubovas, K. and King, A. R. (2014). Galaxy-wide outflows: cold gas and star formation at high speeds. *Monthly Notices of the Royal Astronomical Society*, 439(1):400–406.

Zubovas, K., Nayakshin, S., Sazonov, S., and Sunyaev, R. (2013). Outflows of stars due to quasar feedback. *Monthly Notices of the Royal Astronomical Society*, 431(1):793–798.

Zwicky, F. (1956). Multiple Galaxies. *Ergebnisse der exakten Naturwissenschaften*, 29:344–385.